Received: 16 August 2022 | Revised: 5 December 2022 | Accepted: 2 February 2023

DOI: 10.1002/nme.7218

RESEARCH ARTICLE

WILEY

A robust computational strategy for failure prediction of masonry structures using an improved multi-surface damage-plastic based interface model

Yu Nie | **Abdul Sheikh** | **Phillip Visintin** | **Michael Griffith**

School of Civil, Environmental & Mining Engineering, The University of Adelaide, Adelaide, South Australia, Australia

Correspondence
Abdul Sheikh, School of Civil, Environmental & Mining Engineering, The University of Adelaide, Adelaide, South Australia 5000, Australia.
Email: abdul.sheikh@adelaide.edu.au

Funding information
Australian Research Council, Grant/Award Number: DP190100797; The University of Adelaide through Adelaide Research Scholarship

Abstract

In this study, a new traction-separation based constitutive model for use in finite element simulation of masonry joints under complex loading conditions is developed for cohesive elements. The proposed model is formulated using damage parameters and plastic deformation with mutual couplings, and can accurately simulate the complex nonlinear behaviors of masonry joints considering hardening or softening of strength and stiffness degradation. To enhance the numerical stability of the model, plasticity and damage are separated algorithmically and implemented in two phases. In the first phase, the plastic deformations are treated using a multi-surface plasticity model composed of a smooth hyperbolic yield surface for tension-shear mixed-mode failure and an elliptical cap primarily for the compressive failure. This is implemented in effective stress space and helps restrict the evolution of yield surfaces with no softening, significantly enhancing the efficiency of stress return mapping by the closed point projection method. In addition, an adaptive sub-stepping scheme is adopted to further improve the robustness of the numerical implementation. In the second phase, nominal stresses are computed from the effective stresses using damage parameters. The evolution of these damage parameters is defined in terms of plastic work which is defined by a polynomial form, and is recommended in this study for a better calibration capability. Improvements are made in the formulation of compressive cap including incorporation of hardening of strength and stiffness degradations as these are ignored in existing interface models. This approach helped improve simulation of masonry under cyclic loads with tension-compression transitions. For the structural level applications, the interface model is implemented within a finite element program, which is utilized to simulate failure of a number of masonry specimens under in-plane/out-of-plane monotonic/cyclic loading. The simulated results are rigorously validated with existing experimental data that shows a good potential in modeling masonry structures.

KEYWORDS

cyclic loading, damage-plastic model, FE model, interfacial constitutive model, masonry structures, sub-stepping scheme

1 | INTRODUCTION

Investigation of the behavior of masonry structures is an important work in the area of structural engineering that benefits the maintenance of significant heritage buildings and the design of new architectural buildings.[1] However, the prediction of behaviors of masonry structures is challenging due to inhomogeneity in the system and complex nonlinear material response. Though empirical based approaches[2] can provide an easy solution of this problem, they only give an approximate solution that may not be adequate to assess the safety of large masonry buildings with complex architectural forms. Thus, there is a growing trend towards the use of precise numerical modeling approaches for simulating masonry structures because they are capable of solving complex nonlinear problems.[3–10] In this context, Lourenco[11] has classified the modeling strategies of masonry structures into three groups: (1) detailed micro-modeling,[12] where bricks and mortars are discretely modeled using continuum elements and brick-mortar interfaces are modeled with zero thickness cohesive elements; (2) macro-modeling,[13,14] where bricks and mortars are homogenized as a single continuum utilizing a representative volume element (RVE); and (3) simplified micro-modeling,[15] where bricks are modeled using continuum elements, while cohesive elements are used for mortar joints (entire thickness) and artificial joints placed inside bricks to simulate the potential crack in bricks. Amongst the above modeling strategies, the simplified micro-modeling strategy seems an optimum approach as it can provide a balance between computational efficiency and accuracy, and this approach is adopted in this study. As the nonlinear behavior is predominantly localized in mortar joints, the primary challenge of a simplified micro model is to accurately define the nonlinear interfacial behavior by developing a reliable constitutive model for the cohesive element.

Existing literature shows that damage mechanics and plasticity theory are commonly used for interface models. The use of damage mechanics-based interface models become popular in simulating masonry structures,[16,17] and this is likely due to the availability of such interface models in commercially available finite element (FE) programs such as ABAQUS.[18] However, these interface models[18] do not have the option for frictional resistance which is always found in shear/mode II failure of masonry. Though the frictional contact feature can be used in combination with the interface model to address this issue, it is not a good option as the transition from the softening to the friction regions is not captured well. Moreover, the determination of mixed-mode parameters under complex loading scenarios is problematic due to the lack of experimental results. For mix-mode failure simulation, the Benzeggagh-Kenane fracture criterion[19] along with its default values are commonly used,[16,17] but these values are calibrated from testing of polymer based composite materials. To avoid such issues, Alfano and Sacco[20] developed an interface model incorporating the frictional component in their formulation. However, a damage mechanics-based model does not provide dilation characteristics of mortar bed joints, and this is an important feature observed in real experiments.[21]

On the other hand, the use of plasticity-based interface models is found to be more popular in modeling masonry structures, which may be due their better representation of the mortar failure. One of the earlier models was developed by Lofti and Shing[22] who proposed a single hyperbolic yield surface that can successfully capture the tension-shear mixed mode region without using an addition yield surface for tension cut-off. A more traditional approach was adopted by Scimemi et al.,[23] who used a Mohr-Coulomb type flat surface and another flat surface for tension cut-off. The intersection of these two yield surfaces gives a sharp corner, which needs special attention during numerical implementation since it can lead to convergence problems or incorrect stress returns. As this model[23] does not have provision for checking compression failure, the model was extended further by adding another flat yield surface as a compression cap[24,25] parallel to the surface for tension cut-off. A similar model was introduced by Sutcliffe et al.[10] and Chaimoon and Attard,[26] where the flat compression cap was replaced with a conical surface. A further improvement was made by Lourenco and Rots[15] who used an elliptical surface for the compression-cap that led to a very popular model in masonry modeling. But each of these models[10,15,24–26] have two corners (problematic regions) produced by the three surfaces. The number of corners was reduced to one by taking two hyperbolic surfaces,[7] where one was used as a compression cap. To avoid any corners without sacrificing the compression failure, single closed smooth surface having a tear-drop type shape was proposed[27,28] but the performance of the model was not satisfactory as mentioned by the same researcher[29] who recommended to use a multi-yield surface-based plasticity model.

In general, plasticity-based models appear to be much better but they do not provide for stiffness degradation, which is important in masonry structures subjected to cyclic loading due to load reversal. This limitation has motivated researchers in recent years to develop interface elements considering damage, irreversible plastic deformations, and their possible couplings to have a realistic modeling of masonry joints. One such attempt was made by Spada et al.[9] who used yield surfaces similar to that of Scimemi et al.[23] in addition to similar failure envelopes for defining damage by extending the

concept of plasticity to damage. However, linking these two failure envelops with corners made numerical implementation very cumbersome as it needs checking of 16 different cases during integration of their model at every material point. Minga et al.[24] extended the plasticity model to incorporate damage, but that model does not allow for the hardening that can be observed in compression. Also, the authors of Reference 24 did not clarify how the problems associated with stress return near the corners. The hardening of the compression cap was considered by Xie et al.[25] who developed an interface model, where the formulation is primarily governed by the damage to have a total deformation-based simulation that substituted the return mapping. Yuen et al.[30] proposed a comparatively simple model by using a single yield surface similar to that of Reference 22 along with the forward Euler techniques for explicit integration of their model but did little modifications to accommodate sub-stepping.

In addition to the capabilities of the constitutive models, numerical implementation is another important aspect for the overall modeling success, but this is always challenging because convergence issues in the iterative solution process are often experienced when solving real complex problems. A fully implicit integration technique with closed point projection method (CPPM) is a preferred option in a plasticity-based formulation as this technique is unconditionally stable[31] and provides accurate solution.[32] However, this approach usually involves a Newton–Raphson iterative technique for the stress return mapping procedure, which can be divergent if the deformation increment in a time step is large[33] or when there is a sharp region in a yield surface with high curvatures.[34–36] Furthermore, multi-surface models with corners introduce additional difficulties in achieving convergence since the active yield surfaces need to be updated during iterations and an improper strategy adopted in subsequent steps can led to an incorrect stress update.[37] To address these numerical issues, researchers have adopted different strategies such as the line search method[38–40] to improve convergence stability and accuracy for larger step size and exact/optimized/brute force[38,41,42] for detecting the correct active surfaces near corners of multi-surface plasticity models. Similar to line search method, the sub-stepping technique was adopted by some researchers[43,44] because this technique has a generic character and it is more powerful than the line search method. Sloan[44] implemented this technique for forward Euler integration scheme while Pérez-Foguet et al.[43] did it for backward Euler integration scheme.

Though a number of models possessing different degrees of limitations and capabilities exist in literature, some issues are still unresolved and there is a need for development of a comprehensive interface model for accurate and robust failure modeling of masonry structures with computational efficiency. Such an attempt has been made in this study, by developing a coupled damage-plasticity based interfacial model for masonry joints subjected to mixed mode loading comprised of tension, shear and compression. The main novelty of this work is proposing a robust numerical implementation strategy (by using adaptive sub-stepping scheme in combination with effective stress-based formulation) of a multi-surface plasticity model with damage to overcome diverging issues during simulation of masonry structures with complex nonlinearities. The multi-surface model and the sub-stepping scheme help to enhance the accuracy while the computational efficiency is achieved by the effective stress-based formulation. Moreover, a fully implicit backward Euler integration technique is used to improve accuracy.

The proposed multi-surface based constitutive model includes a smooth hyperbolic yield surface as recommended by Caballero et al.[45] and a compression cap as recommended by Lourenco and Rots.[15] The evolution of damage parameters is defined in terms of plastic work using three newly proposed polynomial expressions for effective representation of their variations. We separated the damage and plasticity components algorithmically and they are implemented independently that helped to improve the robustness of numerical simulation. This is achieved by using an effective stress-based formulation, which helped to eliminate any softening of yield surfaces. For a better representation of the tension-compression transition encountered in cyclic loading, the hardening effect is incorporated with the compression cap. The interface model is implemented within the finite element program (ABAQUS) for simulation of a number of masonry structures under monotonic and cyclic loads applied in the form of in-plane and out-of-plane modes. Finally, a thorough experimental validation of the simulated results is conducted using test data available in literature, which demonstrated a very good performance of the model in analyzing a wide range of masonry structures.

2 | FORMULATION OF THE INTERFACIAL CONSTITUTIVE MODEL

The cracking failure progression in masonry joints (similarly applicable to other quasi-brittle type materials) can be characterized by the stress-relative displacement response at the crack interface as shown in Figure 1. Experimental tests[46,47] under uniaxial tension and simple shear indicate that the inelastic behavior of mortar joints is predominantly a strain softening response, as shown in Figure 1B. The test under uniaxial compression[48] shows a visible strain hardening region

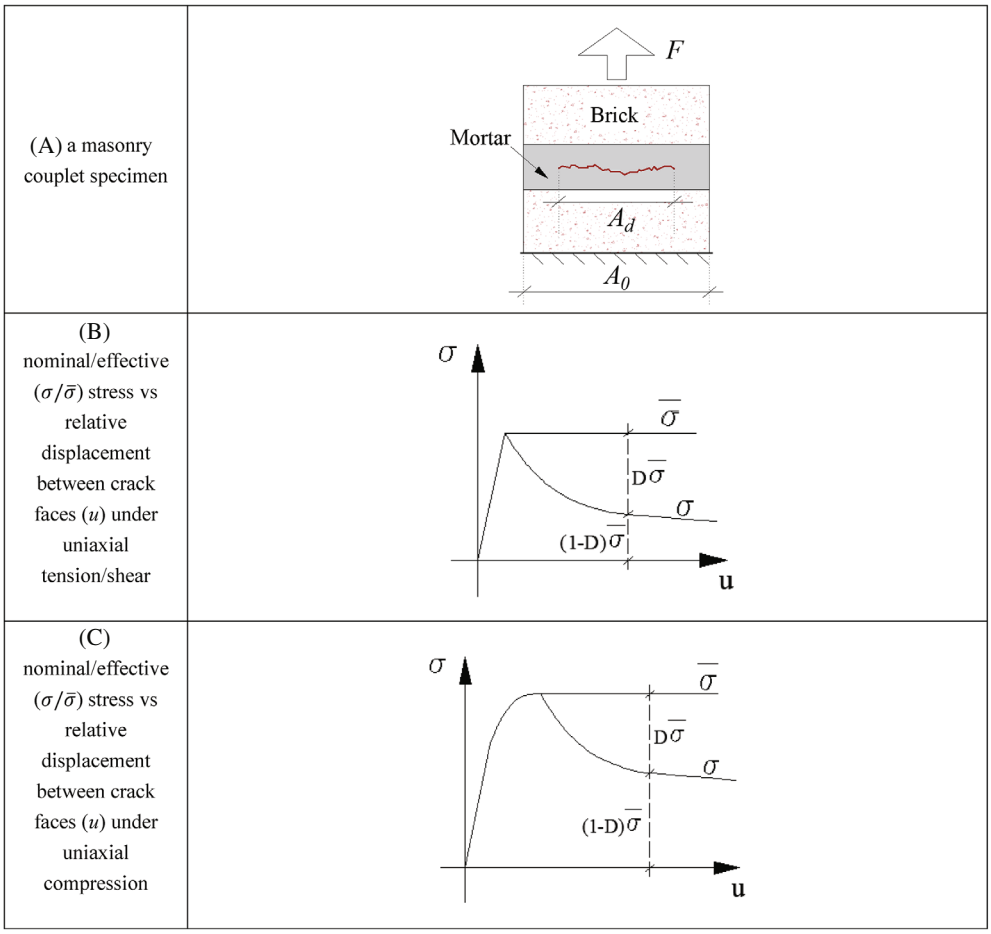

FIGURE 1 Characterization of masonry joint failure with nominal and effective stresses

before the softening response (Figure 1C). As the failure of masonry mortar joints is simulated by an interface model, in this study, the stress is expressed in terms of separation of mortar joints, that is, the relative displacement (u) rather than strain commonly used for continuum models.

During the initial stage of loading after yielding, some micro-cracks are formed in masonry mortar joints or cement matrix as well as the interface between coarse aggregates and cement paste of concrete structures. With the gradual increase of loading F, micro-cracks grow, propagate and joined together to form a macro-crack (see Figure 1A). The degree of failure can be defined using the damage parameter D, which is the ratio of damaged area of the mortar interface A_d to its initial gross area A_0 (Figure 1A). For a damaged joint, the nominal stress and effective stress are defined as $\sigma = F/A_0$ and $\overline{\sigma} = F/(A_0 - A_d)$, respectively, and they can be related using the damage parameter as $\sigma = (1 - D)\overline{\sigma}$. It is to be noted that the value of nominal stress (σ) changes with the change of load (F) only as A_0 is constant while the effective stress ($\overline{\sigma}$) depends on the current load as well as current undamaged area. The formation of micro-cracks degrades the additional load resisting capability that shows strain hardening behavior, which is prominent for compressive loading (Figure 1C). Once the macro-cracks are formed, the load resistance of the material/mortar is dropped that shows a strain softening response (Figure 1B,C). For the tensile and shear loading, the delay between the formations of micro- and macro-cracks is not significant and leads to a negligible strain hardening region. Unlike the nominal stress (that follows the variation pattern of load F), the effective stress remains constant without any drop after the peak load, and this helps to improve the robustness in numerical modeling. The interfacial constitutive model has two stress components and their representations in nominal and effective stress spaces can be related as:

$$\begin{Bmatrix} \sigma_n \\ \sigma_s \end{Bmatrix} = \begin{bmatrix} 1 - D_n & 0 \\ 0 & 1 - D_s \end{bmatrix} \begin{Bmatrix} \overline{\sigma}_n \\ \overline{\sigma}_s \end{Bmatrix}; \quad \{\sigma\} = ([I] - [D])\{\overline{\sigma}\}, \tag{1}$$

where $[I] = \text{diag}\{1, 1\}$ is a unit matrix; subscripts n and s are used to denote the normal and shear components, respectively; and other notations follow the previous descriptions.

In the elastic range of the interface, the traction-separation ($\{\overline{\sigma}\} - \{u\}$) relationship in effective stress space can be expressed as:

$$\begin{Bmatrix} \overline{\sigma}_n \\ \overline{\sigma}_s \end{Bmatrix} = \begin{bmatrix} K_n^0 & 0 \\ 0 & K_s^0 \end{bmatrix} \begin{Bmatrix} u_n \\ u_s \end{Bmatrix}; \quad \{\overline{\sigma}\} = \left[K^0\right]\{u\}, \tag{2}$$

where K_n^0 and K_s^0 are elastic stiffness of the interface interfacial in normal and shear mode deformations.

The formulation for the inelastic response of the proposed interface model involves two stages: plasticity in the first stage and damage evolution in the second stage, which are presented in the following sections.

2.1 | Plasticity formulation of the interface

A multi-surface plasticity models as shown in Figure 2 is used for the proposed interface model. The yield surface of the model consists of a smooth hyperbolic curve F_1 for simulating the behavior under tension-shear mixed mode of loading and an elliptical curve F_2 to simulate the behavior under compression (Figure 2). In the effective stress space, these yield surfaces (F_1 and F_2) can be expressed as:

$$F_1 = -\left(f_s - \overline{\sigma}_n \tan\phi\right) + \sqrt{\overline{\sigma}_s^2 + \left(f_s - f_t \cdot \tan\phi\right)^2}, \tag{3}$$

$$F_2 = C_{nn}\overline{\sigma}_n^2 + C_{ss}\overline{\sigma}_s^2 + C_n\overline{\sigma}_n - f_c^2, \tag{4}$$

where f_t, f_c, f_s, and $\tan\phi$ are tensile strength, compressive strength, shear strength, and frictional coefficient of the interface; C_{nn} and C_{ss} are configuration parameters that control the size of the ellipse (F_2) in normal and shear directions, while C_n determine the positon of the elliptic center on $\overline{\sigma}_n$ axis.

The hyperbolic curve F_1 is adopted from Caballero et al.[45] who proposed a tension-shear mixed-mode interface model within a pure plasticity framework to simulate the cracking failure of concrete materials. In their work, which is based on nominal stress space, the yield surface has a hyperbolic curve and contracts gradually as the material softens, and finally reduces to a conical surface with a sharp corner that can be a source of convergence problems during the stress return mapping. As the present work is based on the effective stress space, the curve F_1 does not contract as its parameters (f_t,f_s, and $\tan\phi$) remain constant and its behavior is similar to an elastic-perfectly plastic model. The elliptic surface F_2 is used for the compressive cap, which is adopted from Lourenco and Rots[15] who proposed a pure plasticity based interface model having Mohr-Coulomb type yield surface with tension cut-off along with the compressive cap. As the model of

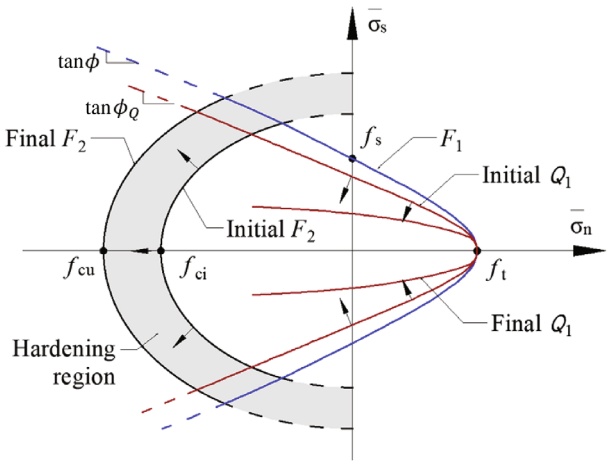

FIGURE 2 Yield and potential surfaces in effective stress space and their possible evolutions

Reference 15 is based on nominal stress space, F_2 will shrink after peak load due the material softening, which can cause numerical instability during the stress return mapping procedure.[39] Grassl and Rempling[49] proposed a model using a single yield surface having a full elliptical shape and formulated their model in effective stress space which helped to minimize the convergence problem due to this numerical instability. This has motivated us to formulate our model in effective stress space that will restrict the evolution of F_2 (present model) in the hardening region only ($f_{ci} \le f_c \le f_{cu}$) in the form of expansion (Figure 2) with no further change or shrinking during the strain softening region after peak load (f_{cu}). The evolution of F_2 in the hardening region only and no evolution of F_1 has helped to enhance the robustness of our numerical implementation.

A typical nonassociated behavior is observed in the post elastic deformation of quasi-brittle materials such as mortar joints or masonry bricks since their dilation angle ϕ_Q controlling the direction of plastic deformation is much smaller than the frictional angle ϕ defining the yield surface. This needs a plastic potential surface Q_1 (Figure 2), different from F_1 (nonassociated), where Q_1 is dependent on dilation coefficient $\tan\phi_Q$ for estimating plastic deformations. However, the compressive cap in present work follows the associated flow rule, thus its potential surface Q_2 is the same as the yield surface F_2 as it does not involve a frictional component of the material response. The expression of the potential surfaces are as follows, where Q_1 is obtained from F_1 (Equation 3) by replacing ϕ with ϕ_Q.

$$Q_1 = -\left(f_s - \overline{\sigma}_n \tan\phi_Q\right) + \sqrt{\overline{\sigma}_s^2 + \left(f_s - f_t \cdot \tan\phi_Q\right)^2}, \tag{5}$$

$$Q_2 = F_2. \tag{6}$$

During hardening of the compression cap, the evolution of the compressive strength f_c needed to define F_2 or Q_2 (Equation 4) is expressed in terms of accumulated plastic work W^p used as internal variable (see Section 2.2). The same internal variable is used to define the evolution of damage parameter needed to estimate the nominal stress of the compression cap from its effective stress in the strain softening range. Similarly, plastic work (dissipated energy) is used to define the evolution of the damage parameter for tension-shear mixed-mode deformation characterized by F_1. In numerical implementation, the integral form of plastic work is computed incrementally as $W^p = \int dW^p = \sum dW^p$ by updating its value after convergence of every load increment. The increment of plastic work dW_1^p and dW_2^p corresponding to the two yield surfaces F_1 and F_2 can be defined as:

$$dW_1^p = \begin{cases} \overline{\sigma}_n du_n^{p1} + \overline{\sigma}_s du_s^{p1}, \overline{\sigma}_n \ge 0, \\ \left|du_s^{p1}\right| \left(\left|\overline{\sigma}_s\right| + \overline{\sigma}_n tan\phi\right), \overline{\sigma}_n < 0, \end{cases} \tag{7}$$

$$dW_2^p = \overline{\sigma}_n du_n^{p2} + \overline{\sigma}_s du_s^{p2}, \tag{8}$$

The estimation of dW_1^p depends on the nature of normal stress σ_n, that is, tension or compression. If the interface is under tension ($\overline{\sigma}_n \ge 0$), the dissipated energy is produced by both normal and shear deformations, while the effect of shear deformation is only considered under compression ($\overline{\sigma}_n < 0$) with a deduction for the frictional component $\left(\left|du_s^{p1}\right| \cdot \overline{\sigma}_n \tan\phi\right)$ since it is not included in characterize the cohesive behavior and related fracture energy in shear. On other hand, the determination of dW_2^p depends on normal and shear modes of deformation and it is not affected by the nature of normal stress. The 2D cohesive model presented above can be easily extended to 3D model by incorporating another shear component and the resulting formulation of the 3D model is presented in Appendix A.

2.2 | Evolution of damage parameters and nominal stresses

Due to heterogeneity in the behavior of mortar-brick joints under different modes of deformation, the degradation of interface strengths during material softening is determined by using three different damage parameters corresponding to tensile (d_t), shear, (d_s) and compressive (d_c) modes of failures. A single scale damage parameter may be conveniently used for continuum models for isotropic material,[50,51] but multiple damage parameters are needed for interfacial based constitutive models[52] or continuum models for anisotropic materials such as wood[42] or composites.[53] The experimental testing of masonry couplet/prism specimens under uniaxial tension,[47] uniaxial shear,[46] and uniaxial compression[48] show dissimilar response in terms of their strengths and fracture energies. The damage parameters used in the present model are expressed in terms of plastic work, fracture energies, material strength parameters, and some additional parameters

controlling the shape of damage evolution (shape parameters) as:

$$d_t = \begin{cases} \alpha_t \left(\frac{W_1^p}{G_{ft}}\right)^{\alpha_t - 1} - (\alpha_t - 1)\left(\frac{W_1^p}{G_{ft}}\right)^{\alpha_t}, & W_1^p < G_{ft}, \\ 1, W_1^p \geq G_{ft}, \end{cases} \tag{9}$$

$$d_s = \begin{cases} \alpha_s \left(\frac{W_1^p}{G_{fs}}\right)^{\alpha_s - 1} - (\alpha_s - 1)\left(\frac{W_1^p}{G_{fs}}\right)^{\alpha_s}, & W_1^p < G_{fs}, \\ 1, W_1^p \geq G_{fs}, \end{cases} \tag{10}$$

$$d_c = \begin{cases} 0, W_2^p \leq G_{fch} \\ \left(1 - \frac{f_{cr}}{f_{cu}}\right)\left[\alpha_c \left(\frac{W_2^p - G_{fch}}{G_{fcs}}\right)^{\alpha_c - 1} - (\alpha_c - 1)\left(\frac{W_2^p - G_{fch}}{G_{fcs}}\right)^{\alpha_c}\right], G_{fch} < W_2^p \leq G_{fc}, \\ \left(1 - \frac{f_{cr}}{f_{cu}}\right), W_2^p > G_{fc}, \end{cases} \tag{11}$$

where G_{ft}, G_{fs}, and G_{fc} are fracture energies for tensile, shear, and compressive modes of deformation; α_t, α_s, and α_c are shape parameters for tensile, shear, and compressive mode of damage evolution; f_{cu} and f_{cr} are ultimate and residual compressive strengths. It is to be noted that the hardening component G_{fch} and the softening component G_{fcs} of G_{fc} $\left(= G_{fch} + G_{fcs}\right)$ are needed separately to express the damage parameter under compression d_c.

With these damage parameters, the damage matrix appeared in Equation (1) can be formed as:

$$[D] = \begin{bmatrix} D_n & 0 \\ 0 & D_s \end{bmatrix}, \tag{12}$$

where

$$D_n = \begin{cases} d_t, & \sigma_n \geq 0 \\ d_c, & \sigma_n < 0 \end{cases} \text{ and } D_s = \begin{cases} d_s, & \sigma_n \geq 0, \\ d_s \frac{f_{s0}}{f_{s0} + |\sigma_n| \tan\phi}, & \sigma_n < 0. \end{cases} \tag{13}$$

In above equation, the expressions of shear damage variable D_s are different in tension (crack opening) and compression (crack closing) since the friction resists the crack growth in shear, while the additional resistance provided by friction increases with the increase of compressive stress and becomes zero in tension.

With the damage parameters, the material strengths (normal and shear) under opening and closing modes of deformation are expressed as:

$$\sigma_n = \begin{cases} f_t = (1 - d_t) f_{t0} \text{ Opening mode}, \\ f_c = \begin{cases} f_{ci} + (f_{cu} - f_{ci})\left(\frac{2W_2^p}{G_{fch}} - \left(\frac{W_2^p}{G_{fch}}\right)^2\right)^{\beta}, W_2^p \leq G_{fch} \\ (1 - d_c) f_{cu}, W_2^p > G_{fch} \end{cases} \text{ Closing mode}, \end{cases} \tag{14}$$

$$\sigma_s = f_s = \begin{cases} (1 - d_s) f_{s0}, \text{Opening mode}, \\ \left(1 - d_s \frac{f_{s0}}{f_{s0} + |\sigma_n| tan\phi}\right) f_{s0}, \qquad \text{Closing mode}, \end{cases} \tag{15}$$

where f_{t0} and f_{s0} are initial strength for tension and shear separately; f_{ci} is the initial compressive strength at the onset of yielding; β is the shape parameter for the evolution of compressive strength during hardening. It should be noted that, unlike other strength parameters, the evolution of compressive strength during hardening is not dependent on damage parameters, but it needs the plastic work and hardening part of the fracture energy apart from the initial and ultimate compressive strengths.

The variations of damage parameters and strengths with respect to plastic work under different modes of uniaxial loading are plotted in Figure 3. The strength parameters are degraded gradually with the increase of damage parameters, which are in turn dependent on the plastic work (W_1^p and W_2^p). For tensile loading, the influence of the shape parameter

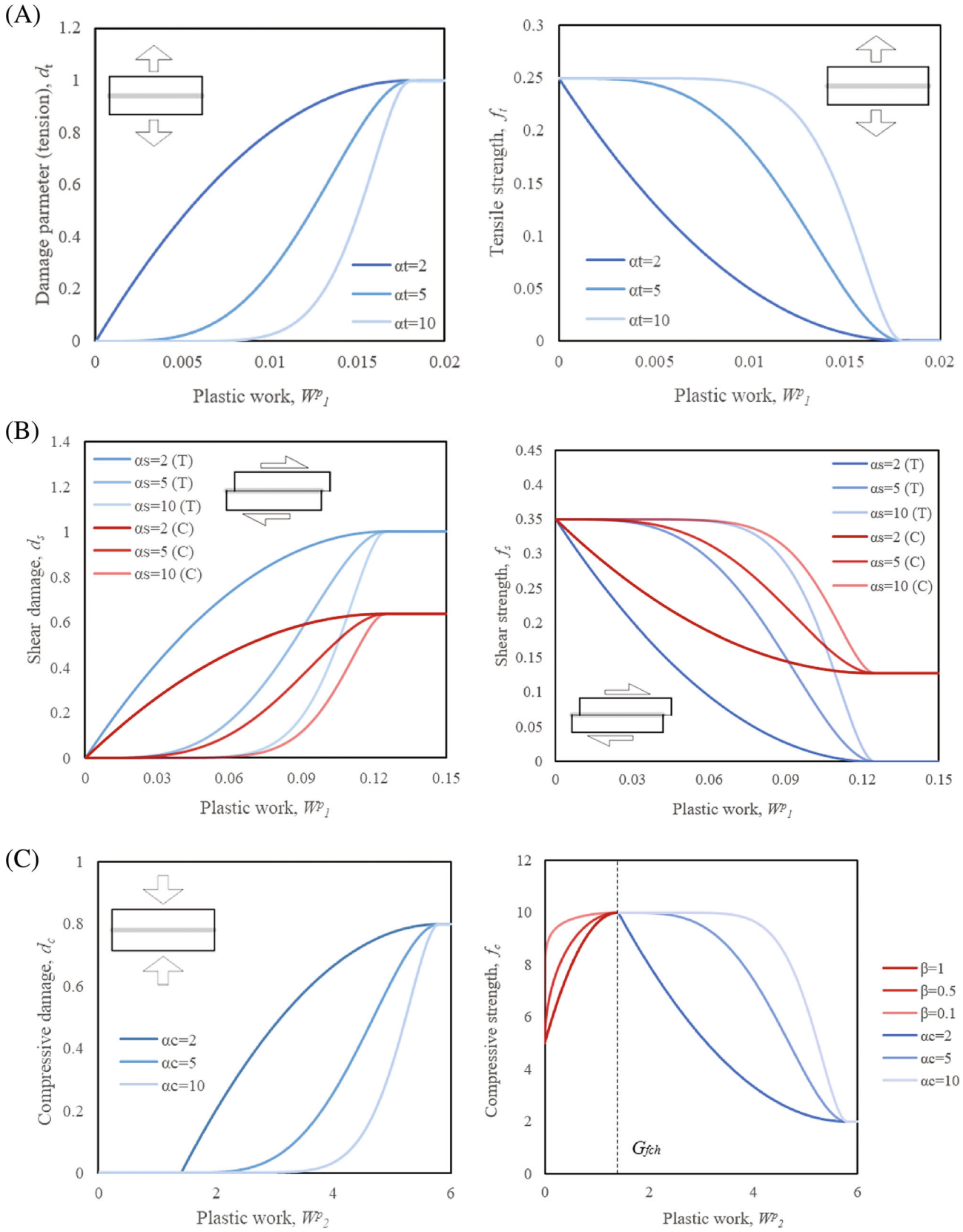

FIGURE 3 Evolution of damage and strength of masonry joints under different modes of uniaxial loading. (A) Evolution of damage and strength under tension, (B) uniaxial shear damage and strength, and (C) uniaxial compressive damage and strength

α_t on the variation of strength is shown in Figure 3A where the rate of strength degradation at the initial stage (lower value of W_1^p) is found to be very small for a higher value α_t. This is absolutely negligible as the curve became initially flat for $\alpha_t > 3$ and the flat region extends with the increase of α_t. This is similarly observed in Figure 3B,C, which demonstrate that shape parameters (α_t, α_s, and α_c) can efficiently help to calibrate the strength parameters in terms of plastic work. Figure 3B shows that the shear strength of the interface decreases to zero when the interface is subjected to tension or no normal loading, while the interface has a residual strength due to frictional resistance ($|\sigma_n| \cdot \tan \phi$) if the interface is under compression.

Figure 3C shows the behavior of the interface under compression, where the curves for the strength evolution are divided into hardening and softening regions at the same point (indicated by the vertical dashed line) when the plastic work W_2^p reaches the value of G_{fch} (portion of the fracture energy under compression corresponds to the hardening part). Also, the hardening curve becomes stiffer with the decrease of the hardening shape parameter β.

It should be noted that, the value of hardening shape parameter β should be 1 or less (not negative) while the softening shape parameters α_t, α_s, and α_c should be 2 and more (may be $+\infty$).

2.3 | Evolution of dilation coefficient

The direct shear tests conducted by Chainmoon[54] on masonry couplets show that the normal displacement of joints caused by the dilation effects was gradually reduced with the shear loading to a small constant value that may be close to zero in some scenarios (Figure 4**)**. This experimental observation indicates that the dilation coefficient $\tan \phi_Q \left(= du_n^p / du_s^p\right)$ has softening characteristics with the progression of shear loading. This effect is incorporated in the present model through a parameter $d_{\phi Q}$ which is used to simulate the degradation of the dilation coefficient $tan\phi_Q$ from its initial and residual values $\tan \phi_{Q0}$ and $\tan \phi_{Qr}$, respectively, as recommended in Equation (16).

$$\tan \phi_Q = \begin{cases} \tan \phi_{Q0} - \left(\tan \phi_{Q0} - \tan \phi_{Qr}\right) d_{\phi_Q}, W_1^p < G_{fs}, \\ \tan \phi_{Qr}, W_1^p \geq G_{fs}, \end{cases} \tag{16}$$

where

$$d_{\phi_Q} = \left[\alpha_{\phi Q} \left(\frac{W_1^p}{G_{fs}} \right)^{\alpha_{\phi Q} - 1} - \left(\alpha_{\phi Q} - 1\right) \left(\frac{W_1^p}{G_{fs}} \right)^{\alpha_{\phi Q}} \right].$$

The above parameter $d_{\phi Q}$ is expressed in terms of plastic work W_1^p, fracture energy under shear G_{fs}, and a shape parameter $\alpha_{\phi Q}$ in the form of a polynomial as recommend in Equation (16). The concept behind the proposed expression for $d_{\phi Q}$ is extracted from the formats used for defining the damage parameters. The variation of $\tan \phi_{Qr}$ with respect to W_1^p is plotted in Figure 5, which shows a similar pattern as found for the damage parameter, that is, the curve becomes more flat in the initial stage with the increase of $\alpha_{\phi Q}$.

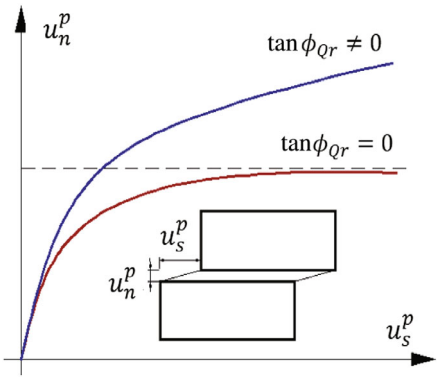

FIGURE 4 Variation of normal displacement versus shear displacement (relative) under shear loading[54]

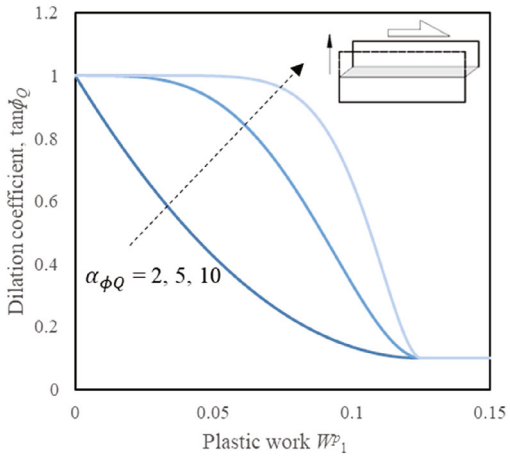

FIGURE 5 Evolution of dilation coefficient with respect to plastic work under shear loading

3 | NUMERICAL IMPLEMENTATION

The effective stress-based formulation used for the proposed model facilitates the separation of damage and plasticity components algorithmically, as mentioned earlier, which helps to improve the computational efficiency and robustness in the implementation of the constitutive model in an incremental-iterative scheme. The main steps associated with its numerical implementation for a load step/increment are listed below and the flow of operation is shown in Figure 6.

Transferring nominal stress $\{\sigma^t\}$ from the converged previous load/time step "t" to effective stress $\left\{\overline{\sigma}^t\right\}$ by using the damage matrix $[D^t]$;

1. From $\left\{\overline{\sigma}^t\right\}$, the effective stress $\left\{\overline{\sigma}^{t+1}\right\}$ and plastic work $W^{p,t+1}$ in the current load/time step "$t+1$" are iteratively computed by using an elastic predictor-plastic corrector strategy until the converged is attained;
2. Using $W^{p,t+1}$, the damage matrix $[D^{t+1}]$ is updated and it is used to calculate the nominal stress $\{\sigma^{t+1}\}$ for the time step "$t+1$."

Figure 7 shows the stress return mapping procedure in the effective stress space for a typical load step. First the trial stress $\left\{\overline{\sigma}^{t+1}\right\}_{\text{trial}}$ is calculated as elastic predictor from $\left\{\overline{\sigma}^t\right\}$, and if it is found outside of the yield surface, that is, $F(^{\text{trial}}\{\overline{\sigma}\}^{t+1}) > 0$, the material is in inelastic stage and a fully implicit backward Euler integration scheme is utilized for the stress return mapping procedure to calculate $\left\{\overline{\sigma}^{t+1}\right\}$. For the tension-shear mixed mode loading scenario, the trial stress $\left\{\overline{\sigma}^{t+1}\right\}_{\text{trial}}$ returns back to the fixed (non-evolving) hyperbolic yield surface F_1 following the closest point

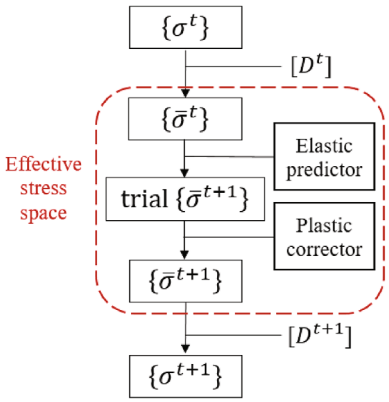

FIGURE 6 Overall process for stress update

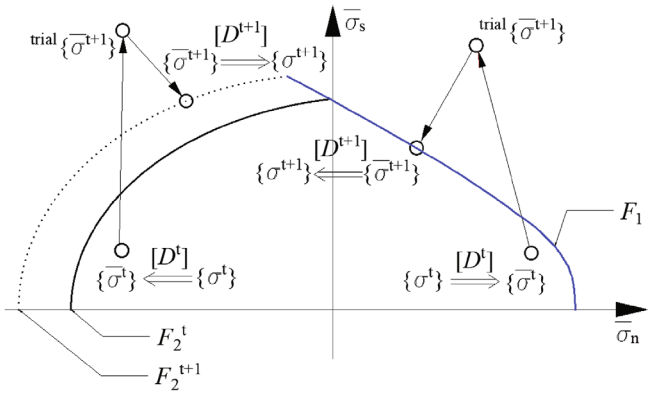

FIGURE 7 Stress return mapping progress

projection method (CPPM) introduced by Simo and Hughes.[37] In case of compression or compression-shear mode of loading, $\left\{\bar{\sigma}^{t+1}\right\}_{\text{trial}}$ returns back to the yield surface F_2 (compressive cap), which can expand (evolve) during hardening stage but remains fixed (not moving) after peak load (see Figure 2).

3.1 | Determination of the correct active surface

For multi-surface plasticity models, a complex scenario is commonly encountered when the trial stress is located near a corner, that is, interaction of multiple yield surfaces, which can lead to wrong stress return mapping due to incorrect selection of yield surface. A typical region near a corner is shown in Figure 8 where the region of the effective stress space can be divided into six subregions (E_L, B_1, B_2, C_1, C_2, A) produced by the yield surfaces F_i (F_1 and F_2 in our model) and their normal (i.e., plastic flow) directions $\partial F_i/\partial\{\sigma\}$. If the trial stress is located within $\mathbf{E_L}$, which is enveloped by the yield surfaces, the stress point is in the elastic domain of the stress space and no stress return mapping is needed and the trial stress (elastic predictor) is the final stress. If the trial stress point is located in region B_2 ($F_1 < 0$, $F_2 > 0$) or region C_2 ($F_1 > 0$, $F_2 < 0$), the correct yield surface will be F_2 or F_1, respectively, that will be used for the stress return. However, both yield surfaces are active in terms of violating yield condition, that is, $F_1 > 0$ and $F_2 > 0$, if the trial stress point is in region B_1, C_1, and A. For a general case of multi-surface plasticity models having any number of yield surfaces, the active set of yield surfaces for a trial set can be expressed as:

$$\{\mathbb{J}_{\text{act}}\} = \{i \in \{1, 2, \dots\} \mid F_i > 0\}. \tag{17}$$

In this scenario, we need to identify the correct yield surface from this set of active surfaces for stress return. A simple solution of this problem has been adopted in some studies (e.g., Reference 7) where the trial stress point belong to all these

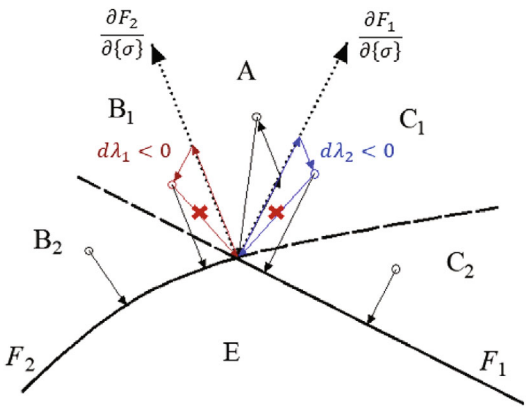

FIGURE 8 Return mapping path of the multi-surface plasticity model

regions (B_1, C_1, and A) predicted by Equation (17) is returned back to the corner. However, this may lead to incorrect stress return that may be significant in some occasions. For example, the trial stress in B_1 should return back to F_2 but not F_1 (see Figure 8). Thus the stress return from the trial stress point belonging to different regions (B_1, C_1, and A) should be treated separately to avoid any issue, which needs identification of the correct region (B_1, C_1, or A).

Therefore, the stress return mapping procedure of multi-surface plasticity models is more challenging than that of single surface plasticity model because the difference of region (B_1, C_1, and A) cannot be distinguished by checking the yield conditions $F_i > 0$ only, that is, Equation (17). Simo and Hughes[37] recommended a generic solution that needs checking of yield conditions $F_i > 0$ as well as plastic multipliers ($d\lambda_i > 0$), which provides a more precise set of active surfaces that can be represented as:

$$\{\mathbb{J}_{\text{act}}\} = \{i \in \{1, 2, \dots\} \, | F_i > 0 \text{ and } d\lambda_i > 0\}. \tag{18}$$

As the stress return is based Newton–Raphson (NR) iterative technique, different strategies may be adopted for determination of $\{\mathbb{J}_{\text{act}}\}$ and these are broadly classified by Pech et al.[42] as follows:

- Exact method: remove a yield surface F_i from the set of active surfaces $\{\mathbb{J}_{\text{act}}\}$ if $d\lambda_i < 0$ but do the checking ($d\lambda_i < 0$) and deactivate F_i only after the convergence of NR iterative method.
- Optimized method: check $d\lambda_i$ after every iteration of the NR iterative method, and update $\{\mathbb{J}_{\text{act}}\}$ by deactivating F_i once $d\lambda_i < 0$ is found.

Another method was proposed by Adhikary et al.[38] that considers all possible combinations of active surfaces. They defined this method as "dumb" as it is not efficient but found it useful in solving a complex scenario with large number of yield surfaces when the above two methods did not work.

There might be a concern with the exact and the above method since they can violate the condition ($d\lambda_i > 0$), but that should be a necessary requirement for feasible solution of a general constrained problem.[55] However, all numerical simulations in this study are solved by the optimized method that worked successfully without facing such an issue.

3.2 | Fully implicit backward Euler integration

The increment of relative displacement $\{du^{t+1}\}$ in current time/load step consists of elastic and plastic components as $\{du^{t+1}\} = \{du^{e,t+1}\} + \{du^{p,t+1}\}$ and it can be used to update the stress as:

$$\begin{aligned}\left\{\overline{\sigma}^{t+1}\right\} = \left\{\overline{\sigma}^{t}\right\} + \left\{d\overline{\sigma}^{t+1}\right\} &= \left\{\overline{\sigma}^{t}\right\} + \left[K^0\right]\left(\left\{du^{t+1}\right\} - \left\{du^{p,t+1}\right\}\right), \\ &= \left(\left\{\overline{\sigma}^{t}\right\} + \left[K^0\right]\left\{du^{t+1}\right\}\right) - \left[K^0\right]\left\{du^{p,t+1}\right\},\end{aligned} \tag{19}$$

where the first part of the above equation provides the trial stress $\left\{\overline{\sigma}^{t+1}\right\}_{\text{trial}} = \left\{\overline{\sigma}^{t}\right\} + \left[K^0\right]\left\{du^{t+1}\right\}$, which is the elastic predictor, while the second part $-\left[K^0\right]\left\{du^{p,t+1}\right\}$ is the plastic corrector. Using the plastic potential functions Q_i, the increment of plastic displacement resultant for multi-surface plasticity model[56] can be determined as:

$$\left\{du^{p}\right\} = \sum_{i \in \{\mathbb{J}_{\text{act}}\}} d\lambda_i \frac{\partial Q_i}{\partial\{\overline{\sigma}\}} \tag{20}$$

where the subscript "i" in above equation corresponds to the set of active yield surface $\{\mathbb{J}_{\text{act}}\}$ which is defined in Equation (18). Substituting Equation (20) into Equation (19), it can be rewritten as:

$$\left\{\overline{\sigma}^{t+1}\right\} = \{^{\text{trial}}\overline{\sigma}^{t+1}\} - \sum_{i \in \{\mathbb{J}_{\text{act}}\}} d\lambda_i^{t+1}\left[K^0\right]\left(\frac{\partial Q_i}{\partial\{\overline{\sigma}\}}\right)^{t+1}. \tag{21}$$

The above equation cannot be solved directly due to nonlinearity, and will be solved iteratively using the NR method that will need updated stress within an iteration as well as updated yield functions or plastic multipliers within that iteration. For the implementation of the iterative technique, the full consistency condition for the yield functions are used and it is expressed as:

$$F_i = 0, i \in \{\mathbb{J}_{\text{act}}\}, \tag{22}$$

where $F_1\left(\left\{\overline{\sigma}^{t+1}\right\}\right)$ is dependent on effective stress only whilst $F_2\left(\left\{\overline{\sigma}^{t+1}\right\}, f_c^{t+1}\right)$ depends on both effective stress and compressive strength.

To facilitate the iterative solution scheme of Equation (21) along with Equation (22), the residual vector $\left\{r^k\right\}$ for k-th iteration can be written as:

$$\left\{r^k\right\} = \begin{Bmatrix} \left\{r_\sigma^k\right\} \\ r_F^k \end{Bmatrix} = \begin{Bmatrix} \left\{\overline{\sigma}^k\right\} - \{^{\text{trial}}\overline{\sigma}^{t+1}\} + \sum_i d\lambda_i^k \left[K^0\right] \left(\frac{\partial Q_i}{\partial\{\overline{\sigma}\}}\right)^k \\ F_i^k \end{Bmatrix}, i \in \left\{\mathbb{J}_{\text{act}}^k\right\}, \tag{23}$$

where a maximum number of iterative "$k_{\max}$" should be predefined to avoid unlimited loops in case of divergence. The converging criteria used in the present study to stop the iteration is defined as:

$$\|r\| = Max(\|\{r_\sigma\}\|, |r_F|) < \text{TOL}, \tag{24}$$

where $\|r\|$ is the norm of residual vector but it is calculated for the two components separately corresponding to Equations (21) and (22) and the larger value is adopted. A small value of the tolerances (TOL) is predefined to stop the iteration with an acceptable level of solution accuracy. The increments of the effective stress vector $\left\{\delta\overline{\sigma}^k\right\}$ and the incremental plastic multipliers $\delta d\lambda_i^k$ (may be a vector but written in the form of index for simplicity in the presentation) within an iteration (k) is written as:

$$\left\{\delta^k\right\} = \begin{Bmatrix} \left\{\delta\overline{\sigma}^k\right\} \\ \delta d\lambda_i^k \end{Bmatrix} = \left[J^k\right]^{-1} \left\{r^k\right\}, i \in \left\{\mathbb{J}_{\text{act}}^k\right\}, \tag{25}$$

where the Jacobian matrix $\left[J^k\right]$ is the gradient of the residual vector (Equation 23) with respect to $\{\overline{\sigma}\}$ and $d\lambda_i$ (the iteration number k is not written for simplicity in the presentation) and it can be expressed as:

$$[J] = \frac{\partial\{r\}}{\partial(\{\overline{\sigma}\}, d\lambda)} = \begin{bmatrix} [I] + \sum_i d\lambda_i \left[K^0\right] \frac{\partial^2 Q_i}{\partial\{\overline{\sigma}\}^2} & \left[K^0\right] \frac{\partial Q_i}{\partial\{\overline{\sigma}\}} \\ \left(\frac{\partial F_i}{\partial\{\overline{\sigma}\}}\right)^T & \frac{\partial F_i}{\partial d\lambda_i} \end{bmatrix}, i \in \left\{\mathbb{J}_{\text{act}}^k\right\}. \tag{26}$$

Using Equation (25), the incremental plastic multiplier and the set of active yield surfaces can be updated as:

$$d\lambda_i^{k+1} = d\lambda_i^k + \delta d\lambda_i^k, i \in \left\{\mathbb{J}_{\text{act}}^k\right\}, \tag{27}$$

$$\left\{\mathbb{J}_{\text{act}}^{k+1}\right\} = \left\{i \in \{1, 2, \ldots\} \mid d\lambda_i^{k+1} > 0\right\}. \tag{28}$$

In some situations, $\left\{\mathbb{J}_{\text{act}}^{k+1}\right\}$ may be changed from its previous iteration $\left\{\mathbb{J}_{\text{act}}^k\right\}$ if one of the incremental plastic multipliers $d\lambda_i^{k+1}$ becomes negative. In that scenario, the new set of active yield surfaces is use and the iteration process is restarted from the beginning of the load step. Otherwise, proceed further after updating the effective stress and the plastic work as:

$$\left\{\overline{\sigma}^{k+1}\right\} = \left\{\overline{\sigma}^k\right\} + \left\{\delta\overline{\sigma}^k\right\}, \tag{29}$$

$$W^{p,k+1} = W_i^{p,k} + dW_i^{p,k}, i \in \left\{\mathbb{J}_{\text{act}}^k\right\}. \tag{30}$$

The plastic work increment dW_i^p in the above equation can be determined by substituting Equation (20) into Equations (7) and (8) is formulated as (iteration number k again omitted for simplicity of presentation):

$$dW_1^p = \begin{cases} d\lambda_1 \left(\sigma_n \frac{\partial Q_1}{\partial \sigma_n} + \sigma_s \frac{\partial Q_1}{\partial \sigma_s}\right), \sigma_n \geq 0, \\ d\lambda_1 \left(|\sigma_s| + \sigma_n \tan\phi\right) \left|\frac{\partial Q_1}{\partial \sigma_s}\right|, \sigma_n < 0, \end{cases} \tag{31}$$

$$dW_2^p = d\lambda_2 \left(\sigma_n \frac{\partial Q_2}{\partial \sigma_n} + \sigma_s \frac{\partial Q_2}{\partial \sigma_s} \right), \tag{32}$$

The numerical implementation of the procedure presented this section is shown in Appendix B.

3.3 | Adaptive sub-stepping scheme for the implicit integration

Even though the implicit integration technique is unconditionally stable, theoretically, for load increments of any size,[31] convergence may be an issue in reality if the integration point is subjected to a complex loading scenario due to some reason such as large curvatures of the yield surface at the tension apex[57] or the size of load step is large. The solution to this problem is the reduction of the load increment size. Though some high-end FE software[18,58] can automatically reduce the load increment, if needed, this is applied globally, that is, all integration points of the whole structure, which significantly affects the computation efficiency. A more efficient and economic strategy is use of sub-stepping scheme in local (material model) level where the reduction of load increment is applied to severely affected integration points only.

As shown in Figure 9, the time step size Δt at global level is sub-divided into a number of sub-steps, which are denoted by $t^m \in [0, 1]$ and the corresponding stresses are denoted as σ^m. The size of a sub-step Δt^m is adaptively adjusted based on the performance of the NR iteration in the previous sub-step using a multiplier δ^m based on the concept of Reference 41, which is defined as:

$$\delta^m = \max\left(\sqrt{\frac{k_d}{k}}, \zeta \right), \tag{33}$$

where k_d is a predefined value which is the desirable number of maximum iterations to achieve convergence and k is the number of iterations utilized in the previous sub-step. If $k < k_d$, the step size adjustment multiplier δ_m will be larger than 1, which indicates that the size of next sub-step will be larger than previous step and vice versa. Another predefined multiplier ζ $(0 < \zeta < 1)$ is used to control the minimum size of a sub-step. This multiplier ζ is directly used to reduce the sub-step size when the NR iteration scheme is failed in addition to calculate δ_m. For the last sub-step, t^m should not exceed 1 and this is achieved by restricting the maximum value of the sub-stepping size as:

$$\Delta t^{m+1} = \min\left(\delta^m \Delta t^m, 1 - t^m \right). \tag{34}$$

Figure 10 shows a flowchart to demonstrate the overview of the adaptive sub-stepping procedure while the detail of its numerical implementation is given in Appendix C.

4 | NUMERICAL ANALYSIS

4.1 | Performance of stress return mapping technique

Before application of the proposed model at the structural scale to problems such as masonry walls, the performance of the model is scrutinized at different levels (material point, single element, and specimen) to have a thorough understanding

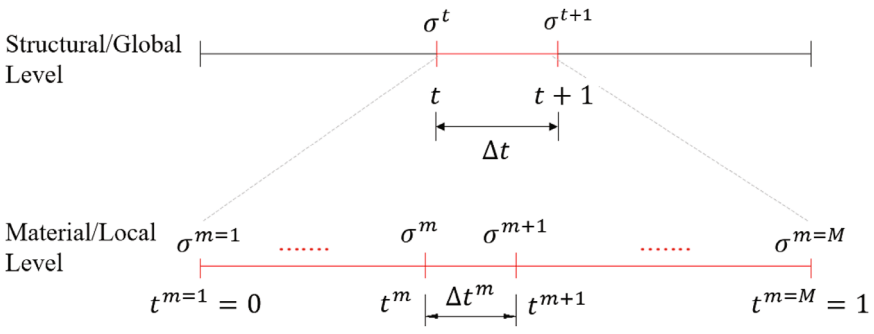

FIGURE 9 Time steps in global (structural) and local (material) levels

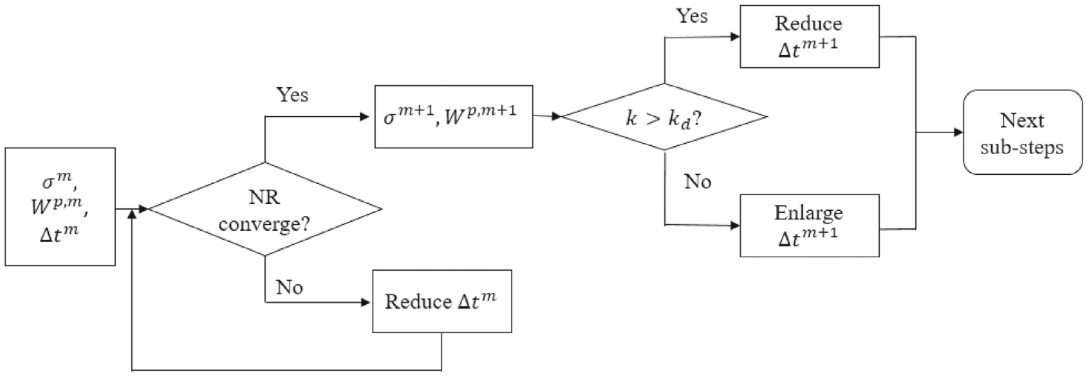

FIGURE 10 Flow-chart for the adaptive sub-stepping procedure

of its performance. In this section, the numerical performance of the model at a material/integration point (i.e., stress return mapping process) is evaluated in terms of efficiency of convergence. A number of stress return mapping tests are numerically conducted with/without sub-stepping to show the importance of sub-stepping. For this purpose, both yield surfaces are assumed to be non-evolving. In this section, the results are presented in schematic form to explain the process, while the actual results for two numerical examples are provided as Supplementary Material (S.2) to provide more detailed results. The stress return mapping technique is implemented numerically by writing a stand-alone program in FORTRAN.

Figure 11 illustrates the different scenarios of stress return mapping process of a trial stress point to the yield surface F_1 where the stress point is located in the region C_2 (see Figure 8) and bit far from F_1. For the first two cases (Figure 11A,B), the sub-stepping option is not be activated, which leads to no convergence in Figure 11A as the stress point oscillated between N1 and N2 with no exit while a convergence is somehow attained in Figure 11B (trial stress point distance is relatively less) but it took a very large number of iterations. Figure 11C shows the use of sub-stepping option for the trial stress in first case (Figure 11A) where a quick convergence is achieved with no numerical trouble. For one of its sub-steps, the return mapping process is illustrated in Figure 11D.

Similarly, the stress return of a trial stress point located in the region B_2 (see Figure 8) is conducted for returning the stress point to the yield surface F_2. In this case, the stress return process performed better than the previous case (Figure 11), which is due to a gentle curvature of F_2 (elliptical curve) while the hyperbolic curve has a high curvature (sharp change) near its tip. However, this took a large number of iterations that may be an issue for solving a large-scale problem. The sub-stepping option is used for the same problem that has shown a significant improvement of the convergence efficiency.

Figure 12 illustrates the stress return paths of a trial stress point located in the region A (see Figure 8) when the sub-stepping option is not used. The stress should go back the corner point but it can drift since the stress point may be moved from region A to B_1 or C_1 (see Figure 8) during the iterative process. This drifting can be avoided by using the sub-stepping option that helps to bring the stress point exactly at the corner. Though the deviation is small, it may be accumulated in a large size complex structural problem.

Before application of the proposed interfacial model to masonry structures, the model is implemented within the finite element (FE) program Abaqus 6.14[18] to investigate its performance using single element (cohesive element COH3D8) test. Results along with the other details are provided as Supplementary Material (S.1).

4.2 | Specimen (couplet/prism) level validation

In this section, the proposed model is validated using couplets and prismatic specimens made of a few bricks, which are subjected to monotonic and cyclic loadings. A brick unit is modeled with solid element (C3D8R) using meshing size of $4 \times 2 \times 2$ while the cohesive elements (COH3D8) is used for mortar joints that followed the meshing arrangement of the bricks. The cohesive elements used the coupled damage-plasticity based constitutive model developed in this study while the bricks are assumed to be elastic. Though the implicit static solver has been used for the single element test, the implicit dynamic solver with a quasi-static mode is adopted from this section to minimize the convergence issue at global/structural level (FE analysis) as the complexity of the problems, need to be simulated, will be increased. For the

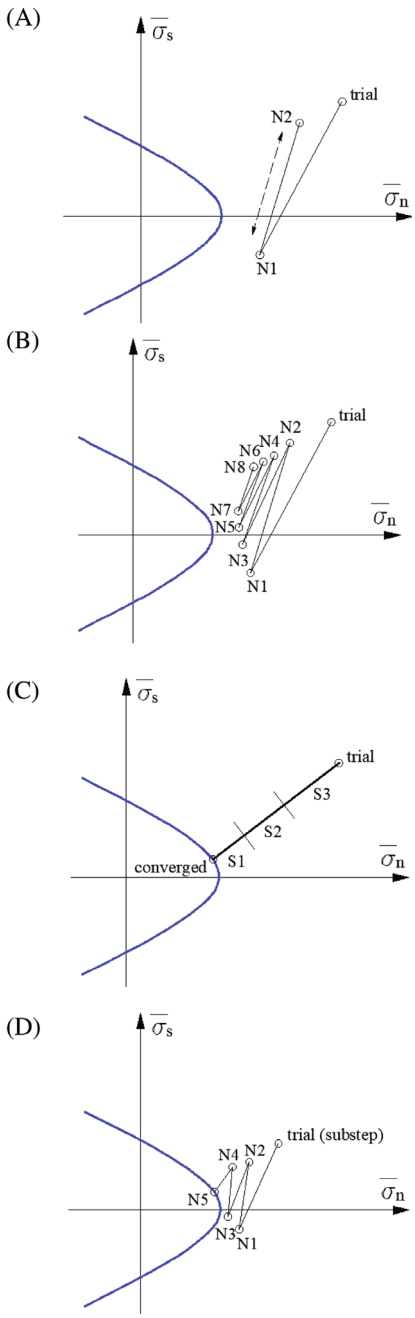

FIGURE 11 Stress return mapping paths corresponding to yield surface F_1.(A) Infinite iteration (no convergence), (B) converged with a large number iteration, (C) sub-stepping scheme, (D) convergence within a sub-step

numerical modeling conduced in this section, the material properties used for the interface are listed in Table 1. The density used for the mortar joints as well as brick and are 2000 kg/m^3 but it is appropriately scaled internally by the quasistatic option of the ABAQUS solver.[18] Material properties used in numerical modeling are collected from experimental literature[46,47,54,59,60] and some parameters are calibrated based on other studies[11,28,30,54,60] which simulated the same experiments.

A displacement controlled tension test was performed by van der Pluijm[47] on clay brick masonry couplets each made of two brick units (size of a unit: 210 mm × 80 mm × 100 mm) and a 10 mm thick mortar joint between the units (Figure 13A) where 80 mm is the height. The experimental results (post elastic softening response) reported by van der Pluijm[47] are presented in Figure 13A for the validation of numerical results predicted by the proposed model for the same problem (uniaxial tension test of the masonry couplet). The numerical results are mostly enveloped within the measured test data set. Similarly, the direct shear tests were conducted by van der Pluijm[46] on masonry couplets having same geometry and

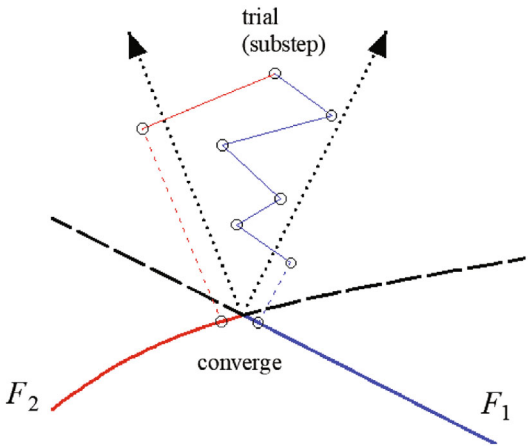

FIGURE 12 Stress return mapping paths for the corner region

TABLE 1 Material properties of the mortar joints for couplet/prismatic specimens

Material parameters	Unit	Uniaxial tension (T)	Uniaxial shear (S)	Cyclic shear (S-Cyc)	Compression (un/re-loading) (C-UR)	Shear (un/re-loading) S-UR, Pv = −0.28 MPa	Shear (un/re-loading) S-UR, Pv = −0.51 MPa
K_n	N/mm^3	82	-	-	300	-	-
K_s	N/mm^3	-	400	36	-	10	4.25
f_{t0}	MPa	0.3	-	-	-	-	-
G_{ft}	N/mm	0.035	-	-	-	-	-
α_t		2	-	-	-	-	-
f_{s0}	MPa	-	1.2	1.2	-	0.07	0.3
$\tan\phi$		-	1	0.67	-	0.82	0.76
G_{fs}	N/mm	-	0.25	3.78	-	0.082	0.14
α_s		-	2	2	-	2	2
f_{ci}	MPa	-	-	-	2	-	-
f_{cu}	MPa	-	-	-	29	-	-
f_{cr}	MPa	-	-	-	2	-	-
G_{fch}	N/mm	-	-	-	8	-	-
G_{fcs}	N/mm	-	-	-	20	-	-
β		-	-	-	0.5	-	-
α_c		-	-	-	3	-	-
$\tan\phi_{Q0}$		-	1	0.1	-	0.15	0.15
$\tan\phi_{Qr}$		-	0.1	0.01	-	0.065	0.001
$\alpha_{\phi Q}$		-	2	2	-	2	4

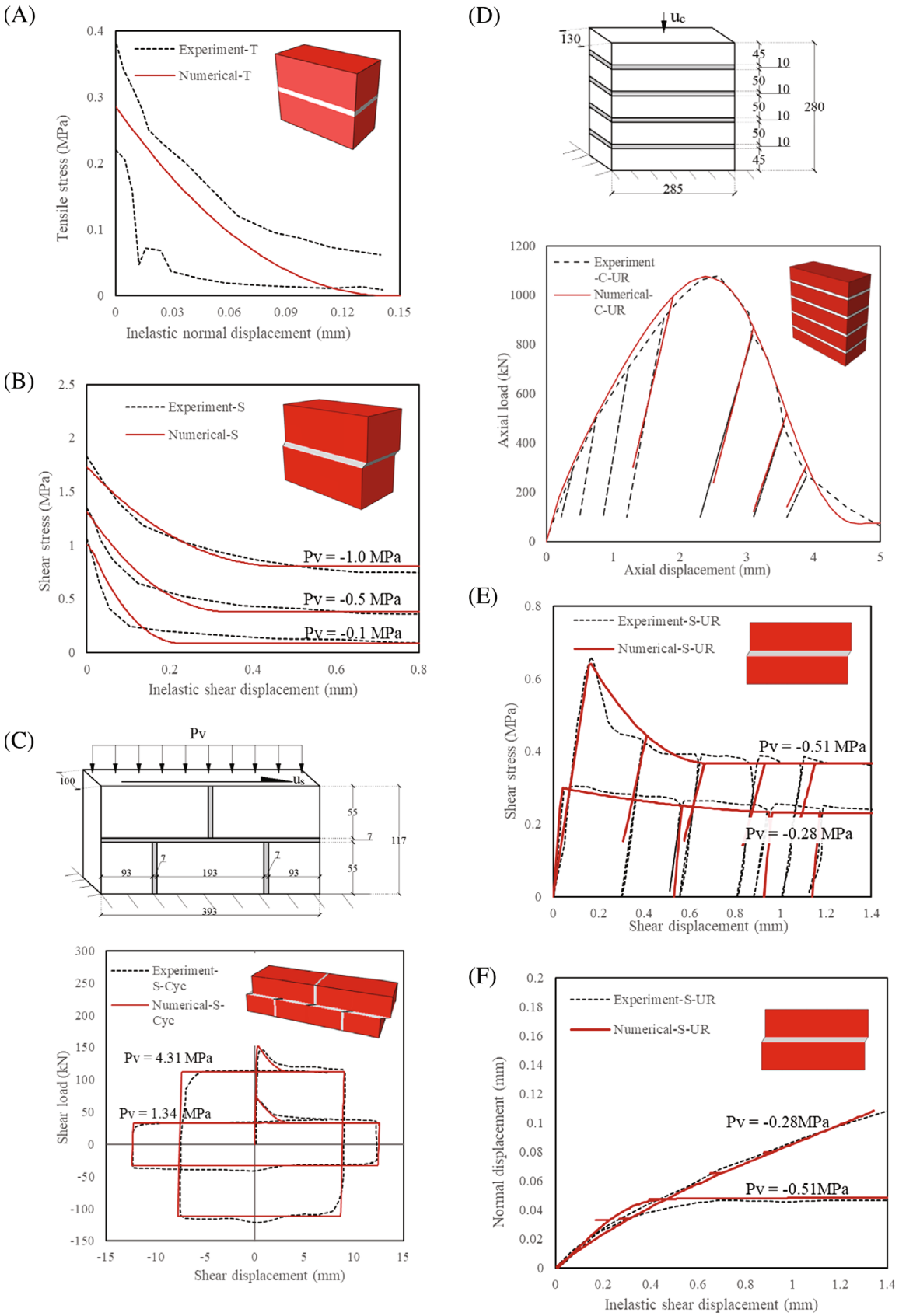

FIGURE 13 Masonry couplet tests. (A) Uniaxial tension, (B) uniaxial shear, (C) cyclic shear, (D) compression, (E) shear stress versus shear displacement, and (F) normal displacement versus shear displacement

materials by imposing three different levels of constant pre-pressure (0.1, 0.5, and 1.0 MPa) applied vertically. The couplets under this loading scenario are simulated with the proposed model and the predicted results are presented with the test results[46] in Figure 13B for experimental validation. The variation of shear stress with respect to the inelastic displacement (Figure 13B) shows an exponential softening followed by a constant residual friction. In the numerical modeling, the values of the shape parameters α_t and α_s are taken as 2 to simulate the exponential softening as observed in the experiment. Figure 13B shows a good correlation between the numerical and experimental results.

Atkinson et al.[59] performed cyclic shear tests on masonry bed joints having a different size and configuration as shown in Figure 13C using two levels of constant pre-pressure (1.34 and 4.31 MPa) for a complete cycle. The numerical simulation of these specimens are conduced by the proposed model, and the predicted results (shear stress-relative displacement variation) are validated with the experimental results[59] in Figure 13C. Modeling results have a good agreement with experiments in terms of peak load and residual frictional resistance.

The performance of the interface model under uniaxial compression with unloading/reloading scenarios for estimating stiffness degradation is validated with the experiment results of Reference 60. A prismatic specimen consisting of 5 bricks as shown in Figure 13D was subjected to vertical compressive load by using a steel plate bonded to the top surface of the specimen that was resting at its bottom surface on a fixed plate.[60] The numerical resulted produced by the proposed model are compared with the experimental results in Figure 13D. Since the stiffness degradation is not observed experimentally during strain hardening region, the unloading-reloading scenario is simulated by the proposed model for one time only before the peak load which has shown the expected behavior of no stiffness degradation. In the softening phase, the unloading/reloading scenario is simulated by the model for three cycles, as was done in experiment, and the results show a stiffness reduction consistent with the experimental response.

The dilation of a masonry joint is now studied by the proposed model that followed the experimental investigation of Reference 54. They applied shear loading on masonry couplets, made of two full size clay bricks (each: 230 mm × 51 mm × 110 mm) connected by a 10 mm thick mortar joint, keeping the couplets under constant pre-pressure having two different values of (0.28 and 0.51 MPa), which show a distinct variation of dilation behaviors. For the specimen under lower confining pressure (0.28 MPa), the peak shear strength was marginally higher than the residual frictional resistance (Figure 13E) while the normal displacement increased steadily with the tangential shear deformation (Figure 13F). In the case with higher pre-pressure (0.51 MPa), the peak strength was visibly higher than the frictional resistance (Figure 13E) while the variation of normal displacement stopped quickly and became nearly flat once the frictional resistance was reached (Figure 13F). The numerical results simulated by the proposed model are compared with the experimental results in Figure 13, and show that the model is capable of capturing all these features with a satisfactory agreement with experimental results. The unloading-reloading scenarios are also simulated as done in the experiment[54] but it shows no stiffness degradation under this mode of loading.

4.3 | Masonry walls under monotonic in-plane and out-of-plane loads

The testing of masonry wall specimens under monotonic in-plane loading, conducted by Reference 61 is widely used as a benchmark example for experimental validations of numerical models and such an attempt is made in this section to assess the performance of our model. For this purpose, three masonry wall specimens, as shown Figure 14A, are adopted from this study[61] who designated them as J4D, J5D, and J7D. These three single leaf wall panels have a geometry (990 mm width × 1000 mm height × 100 mm thickness) composed by 18 courses of solid clay bricks (each: 210 mm × 52 mm × 100 mm) and 10 mm thick mortar joints. The bottom surface of these walls is fully restrained at the ground and the top surface (connected with a steel beam) is subjected to a constant confining pressure (Pv = 0.3 MPa for J4D and J5D; Pv = 2.12 MPa for J7D) and a horizontal load imposed through the steel beam in the form of displacement control.

In our FE modeling of the masonry walls, artificial joints/interfaces are placed through vertical planes of full size bricks at their middle lengths to simulate the potential cracks of brick units as shown in Figure 14B apart from the real mortar joints. For both type of joints, the material properties referenced from References 7,11,24,52 used for the numerical modeling are listed in Table 2. Similar to the previous section, all nonlinear inelastic behaviors of the masonry walls are simulated by the interface model while the bricks (and half bricks) are treated as elastic with Young's modulus $E = 16{,}700$ MPa and Poisson's ratio $\nu = 0.18$. Though the results presented in the previous section corresponds to a mesh size based on 4 × 2 × 2 for single brick unit, it was observed from a mesh convergence study that a relatively less refined

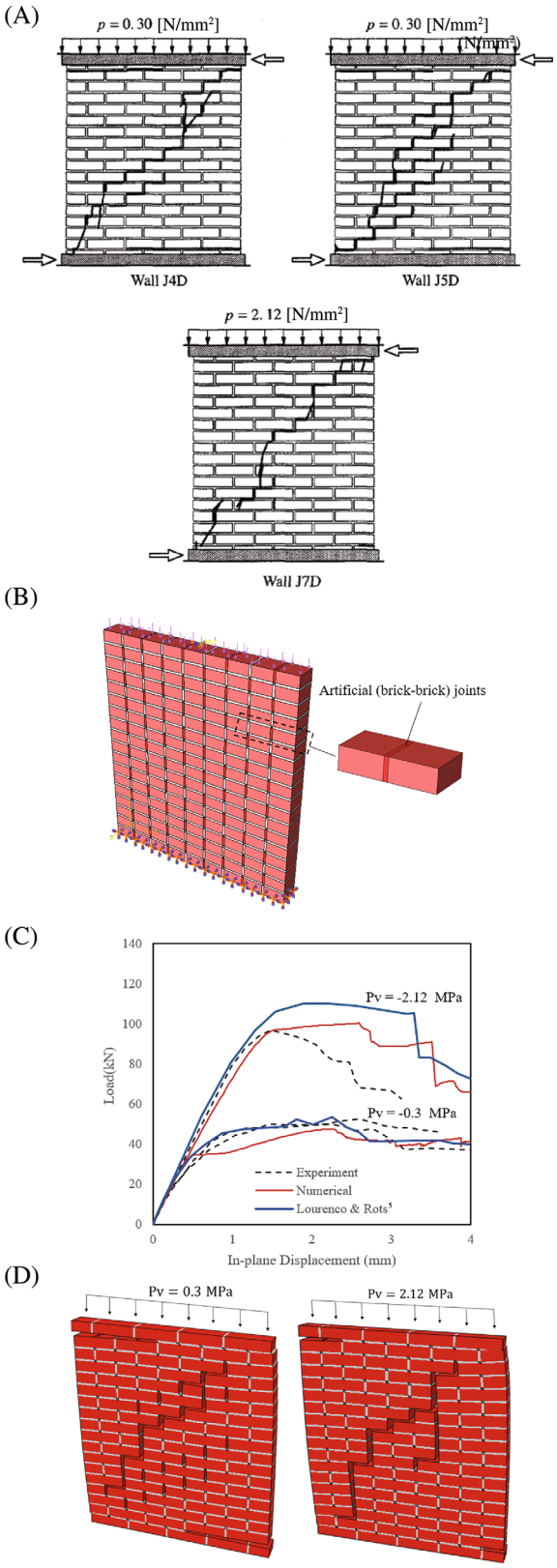

FIGURE 14 Masonry wall panels under monotonic in-plane loading. (A) Masonry wall panels and their failure modes from experiment,[61] (B) FE mode, (C) lead displacement response, and (D) simulated cracking patterns

TABLE 2 Interfacial material properties of the masonry walls under monotonic loading

Material parameters		In-plane loading (Pv = −0.3 MPa)		In-plane loading (Pv = −2.12 MPa)		Out-of-plane loading	
Joints	**Unit**	**Mortar**	**Artificial**	**Mortar**	**Artificial**	**Mortar**	**Artificial**
K_n	N/mm^3	82	100	82	100	220	280
K_s	N/mm^3	36	100	36	100	105	280
f_{t0}	MPa	0.3	2	0.16	2	1	2
G_{ft}	N/mm	0.072	0.12	0.012	0.25	0.072	0.25
α_t		2	2	2	2	2	2
f_{s0}	MPa	0.45	2.8	0.224	4	1.2	2.8
$\tan\phi$		1	1	0.75	1	0.5	1
G_{fs}	N/mm	0.15	0.5	0.05	1	0.25	0.5
α_s		2	2	2	2	2	2
f_{ci}	MPa	2	10	6.5	30	5	30
f_{cu}	MPa	5.5	20	10.5	50	10	50
f_{cr}	MPa	1	5	1	5	2	10
G_{fch}	N/mm	0.8	10.5	2	20.5	10.5	25
G_{fcs}	N/mm	4.2	10.5	3	20.5	10.5	25
β		1	1	1	1	1	1
α_c		2	2	2	2	2	2
$\tan\phi_{Q0}$		0.01	1	0.01	1	0.5	1
$\tan\phi_{Qr}$		0.01	1	0.01	1	0.1	1
$\alpha_{\phi Q}$		2	2	2	2	2	2

meshing can be adequate for getting good results. Therefore, a meshing arrangement based on $2 \times 1 \times 1$ for a single brick unit is adopted in this section for analyzing bigger size problems (walls) with a good degree of computational efficiency.

Numerical results for the load–displacement response at the wall top surface (horizontal direction) simulated by the model are compared with the experimental results in Figure 14C, which shows a good predictive capability of the model for such complex problems. For walls under lower confining pressure (0.3 MPa), the peak load is around 50 kN with a long flat plateau proving a good degree of durability, while the wall under higher confining pressure (2.12 MPa) resisted a higher peak load of around 100 kN but it lost strength rapidly in the post-peak region. Modeling result in this study is compared with that from Reference 15. Figure 14C shows that the post-peak branch predicted by the numerical model has a moderate softening compared to the experimental result. This is probably due to the elastic modeling of the bricks with a single "artificial" vertical interface that attempted for capturing all the nonlinearity of the brick units to reduce the computing time. This modeling strategy allows step-wise cracks with vertical and horizontal cracking planes, which can provide higher strength/stability than brick with inclined cracking. This may be addressed by using an inelastic modeling of the bricks such as concrete damage-plasticity or XFEM based modeling.

Cracking patterns produced by the numerical models (Figure 14D) show typical diagonal cracks go through the entire walls with small horizontal cracks near the corners. Cracks produced by the FE models include failure of mortar (bed and head) joints as well as splitting of bricks though the artificial joints, which helped to simulate the real failure patterns of the walls well.

The capability of the model to simulate the response of masonry walls subjected to out-of-plane monotonic loading is now assessed. For this purpose, a masonry wall panel tested by Ng[62] is adopted. The single leaf wall specimen has 795 mm width, 1190 mm height and 53 mm thickness and was built with solid clay bricks (each: 112 mm × 36 mm × 53 mm) and 10 mm thick mortar joints. In the experimental set-up, an airbag was placed between the masonry wall (back surface) and a stiff support (concrete wall) to provide lateral (out-of-plane) pressure on the back surface of the panel. Four edges of the masonry wall were firmly supported by using a steel frame (Figure 15A) that cause deformation of the wall under two-way bending (Figure 15B). The meshing pattern used for the FE modeling of the wall is identical to that used in the previous

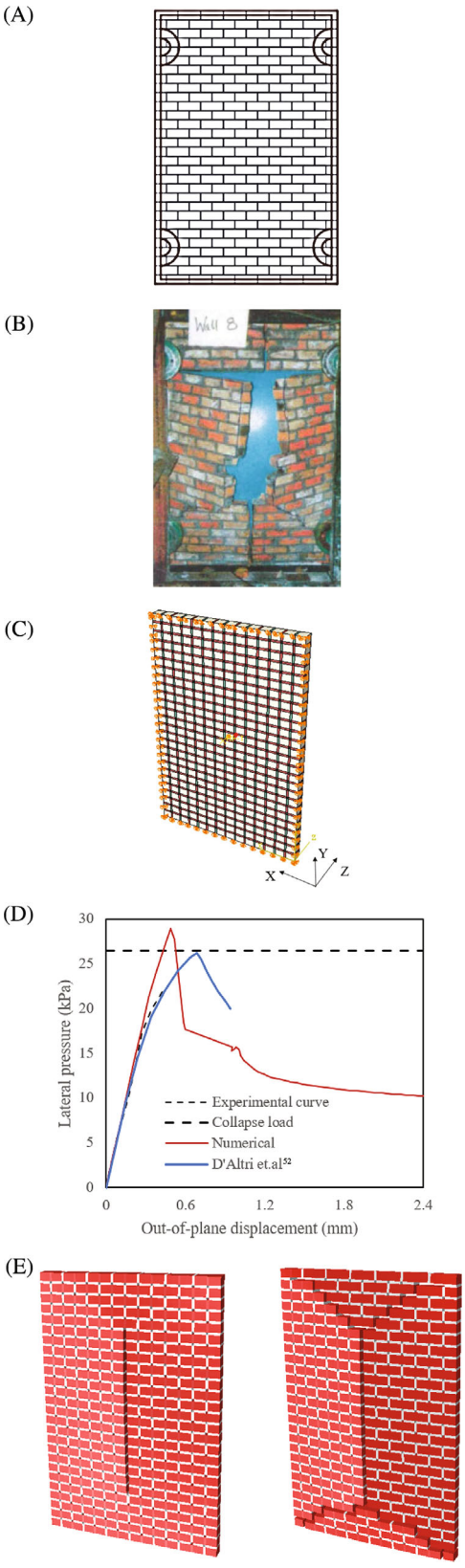

FIGURE 15 A masonry wall panel subjected monotonic out-of-plane loading. (a) a steel frame to support the panel at four edges, (B) failure mode of the wall, (C) FE model of the wall with boundary conditions and RP, (D) load-displacement response, and (E) cracking patterns

case (Figure 14). To simulate the uniform pressure exerted by the air-bag on the wall, a reference point (RP) is used and it is coupled with the loading surface of the panel using the feature "structural distributing" of ABAQUS (Figure 15C). A displacement control technique is applied to the RP that helped to develop pressure on the panel surface but the pressure will be automatically increased or decreased depending on the load resisting capability of the panel during its entire loading range with both hardening and softening behaviors. The material used for the interfaces are same as provided in Table 2 while the bricks are taken as elastic with elastic modulus $E = 16{,}700$ MPa and Poisson's ratio $\nu = 0.15$.

The load–displacement response (deflection at the panel central vs. uniform pressure) predicted by the model is plotted in Figure 15D. For its experimental validation, the measured response as reported by Reference 62 is included in Figure 15D. However, the entire range of the panel response could not be measured experimentally due to unexpected sudden failure of the LVDT before reaching the peak load. Ng[62] could however measure the peak load which is also

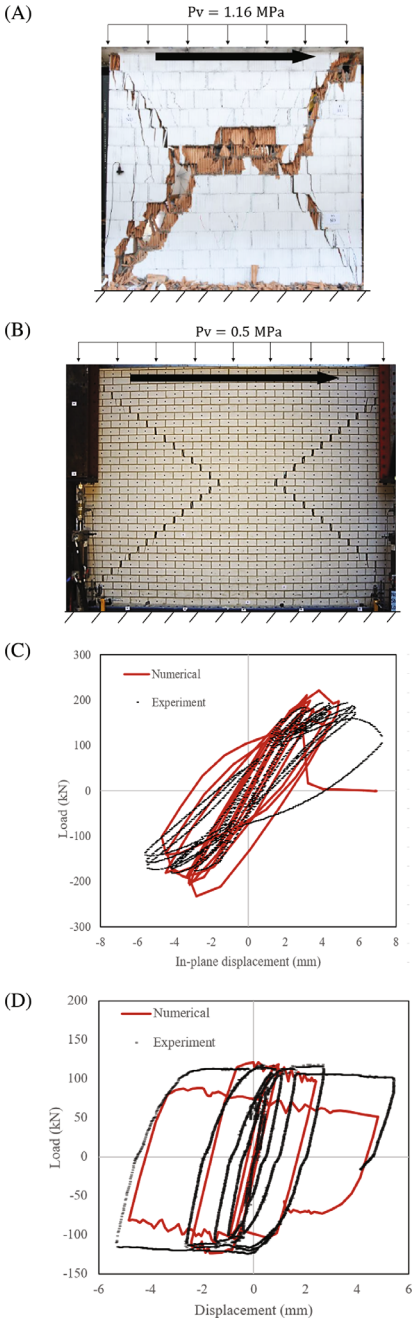

FIGURE 16 Masonry walls under cyclic in-plane loading. (A) T3-ETH, (B) COMP4 - TUD, (C) load-displacement response (ETH wall), and (D) load-displacement response (TUD wall)

included in Figure 15D. The figure shows that the numerical results have a satisfactory correlation with the peak load and the load–displacement response that could be measured. Modeling result is compared with that from Reference 52. Figure 15E shows the failure modes simulated by the model at two different stages of loading. First the straight vertical crack along the longitudinal central line of the panel is produced, and it is then propagated diagonally in four branches from the vertical crack tips to the four corners of the wall.

4.4 | Masonry walls under in-plane cyclic loading

In this section, two single leaf masonry wall specimens subjected to cyclic in-plane loading are selected from literature for experimental validation of the proposed model. Figure 16A shows one of these specimens that was tested by Salmanpour et al.[63] in Swiss Federal Institute of Technology (ETH) Zurich under constant pre-pressure of 1.16 MPa. The wall designated as T3[61] had a dimension of 1590 mm × 1550 mm × 150 mm that was made of 13 courses of clay bricks (each: 250 mm × 190 mm × 150 mm) and 10 mm thick mortar joints. The other wall specimen as shown in Figure 16B was tested under 0.5 MPa pre-pressure by Messali et al.[64] in the Delft University of Technology (TUD). This wall (designated as COMP4) had a dimension of 4000 mm × 2760 mm × 102 mm that was made by 34 courses of calcium silicate bricks (210 mm × 71 mm × 102 mm) and 12 mm mortar joints. Both walls were firmly supported at their bases and subjected to horizontal reversible displacements through a steel beam perfectly bonded at their upper surfaces.

For the FE modeling of these two walls, the meshing system followed the same strategy used in the previous example (Section 4.3). The material properties referenced from References 25, 65 used for the interface modeling are listed in Table 3 while the elastic properties taken for the bricks are: $E = 3000$ MPa and $\nu = 0.2$ for the ETH wall; $E = 9000$ MPa and $\nu = 0.14$ for the DUT wall. Based on the suggestion of Reference 25, different interfacial properties are taken for head and bed joints (mortar) in the present case of cyclic loading.

TABLE 3 Interfacial material properties of the walls subjected to in-plane cyclic loading

Material parameters	Unit	IP-Cyc-ETH (Pv = −1.16 MPa)			IP-Cyc-DUT (Pv = −0.5 MPa)		
Joints		**Mortar-head**	**Mortar-bed**	**Artificial**	**Mortar-head**	**Mortar-bed**	**Artificial**
K_n	N/mm^3	50	20	100	100	10	100
K_s	N/mm^3	25	10	100	40	16	100
f_{t0}	MPa	0.2	0.2	2	0.1	0.01	2.2
G_{ft}	N/mm	0.1	0.1	1	0.05	0.025	0.03
α_t		2	2	2	2	2	2
f_{s0}	MPa	0.45	0.24	2.8	0.14	0.02	1.5
$\tan\phi$		0.3	0.48	1	0.46	0.43	0.46
G_{fs}	N/mm	1.5	1.5	2	3	0.05	0.05
α_s		5	5	2	2	2	2
f_{ci}	MPa	5	2	30	4	6	30
f_{cu}	MPa	9.5	5	50	6	8	50
f_{cr}	MPa	1	1	10	2	2	10
G_{fch}	N/mm	2.5	0.8	25	7.5	17	10.5
G_{fcs}	N/mm	2.5	2	25	7.5	17	10.5
β		1	1	1	1	1	1
α_c		2	2	2	2	2	2
$\tan\phi_{Q0}$		0.1	0.1	1	0.1	0.02	0.36
$\tan\phi_{Qr}$		0.01	0.01	1	0.01	0.01	0.01
$\alpha_{\phi Q}$		2	2	2	2	2	2

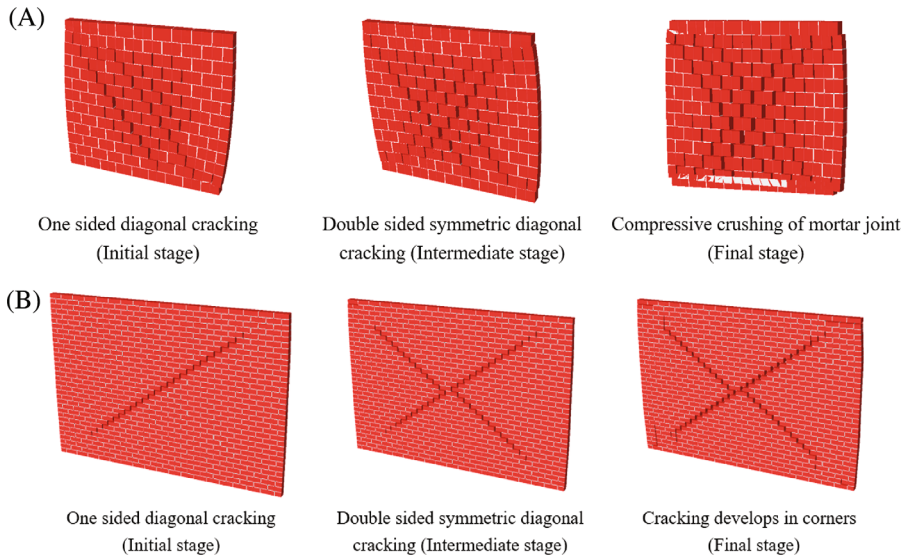

FIGURE 17 Cracking patterns of FE models under cyclic in-plane load. (A) T3-ETH and (B) COMP4 - TUD

The cyclic response (horizontal displacement at top surface vs. load) of the two walls predicted by the proposed model is compared with the experimental results in Figure 16C,D, which show a reasonable consistency between them in terms of peak load and overall hysteretic behavior for such a complex loading scenario.

The gradual degradation of stiffness with the increase of cycles was observed in the ETH masonry panel during experiment, which was due to the compressive crushing failure of mortar bed joints near the bottom edge. This has been successfully captured by the numerical model in Figure 16C. The failure modes of the two walls predicted by the FE model are presented in Figure 17. Figure 17A clearly shows complete crushing of mortar joints near the bottom edge that lead to drop the load resting capacity to zero (see Figure 16C). In contrast, the experiment as well as the FE modeling (Figure 16D) show insignificant stiffness degradation of the TUD masonry wall probably due to lower pre-compression. The simulation shows a typical shear failure mode of the wall (TUD) with two symmetric localized diagonal cracks up to the final stage of loading (Figure 17B), which is similarly observed in experiment (Figure 16B).

5 | CONCLUSIONS

The present study has developed an accurate and robust interfacial constitutive model for masonry joints for use in predicting the nonlinear response of masonry walls subjected to monotonic and cyclic loads applied either in- or out-of-plane. The interface model is implemented within a reliable finite element program (ABAQUS) for failure modeling of structural level problems under complex loading scenarios. The major contributions of this work includes incorporation of damage within a multi-surface plasticity framework in a consistent manner to accommodate strength hardening/softening as well as stiffness degradation of masonry joints subjected to tension, shear, compression or a mixed mode of loading. A smooth hyperbolic yield surface is used to capture the tensile-shear mixed mode behavior. The other yield surface of the plasticity model is an elliptic cap for simulating the compression-shear mixed model scenarios. The interface model is formulated in effective stress space that helped to provide no softening of the yield surfaces and it leads to enhance the robustness of the model by improve the numerical stability.

In the numerical implementation of the interfacial model, a fully implicit backward Euler integration technique is used to achieve enhanced accuracy and robustness in the NR iterative process for the stress return mapping. For a multi-surface plasticity model, the strategy for selection of active yield surfaces and their updating within the iterative process is very important and it has been addressed carefully in this study. To improve the robustness of numerical implementation, an adaptive sub-stepping method is adopted here. Moreover, to enhance the computational efficiency and robustness, an adaptive sub-stepping scheme is implemented that can adjust the load increment size at local (material point) level automatically based on the performance of NR iteration in previous sub-steps.

The performance of the interface model is investigated by analyzing masonry structures in different scales and loading scenarios. This is facilitated with the finite element (FE) modeling of these masonry structures that utilized solid elements for bricks, and cohesive elements for mortar joints as well as artificial joints within brick units. Apart from making some initial checks at the material point and single element level, the different problems simulated by the FE model are: (1) masonry couplets/prismatic specimens under tension, compression and shear with constant pre-compression where these loads may be monotonic or cyclic and may have unloading-reloading scenarios; (2) masonry panels under in-plane and out-of-plane monotonic loads; and (3) masonry walls under in-plane cyclic loads. A thorough experimental validation of the load-deformation response and failure modes of these structures predicted by the model is conducted using benchmarking test results available in literature. The numerical analysis confirmed a very good performance of the model in solving such complex problems of masonry system in terms of accuracy, robustness, and computational efficiency.

ACKNOWLEDGMENT

The first author would like to acknowledge the financial support provided by The University of Adelaide through Adelaide Research Scholarship. This work was supported by Australian Research Council [ARC Discovery (2019–2021), DP190100797]. Open access publishing facilitated by The University of Adelaide, as part of the Wiley - The University of Adelaide agreement via the Council of Australian University Librarians.

DATA AVAILABILITY STATEMENT

The data that support the findings of this study are available from the corresponding author upon reasonable request.

ORCID

Abdul Sheikh https://orcid.org/0000-0002-2839-1707

REFERENCES

1. Tralli A, Alessandri C, Milani G. Computational methods for masonry vaults: a review of recent results. *Open Civil Eng J*. 2014;8:272-287.
2. Theodossopoulos D, Sinha B. A review of analytical methods in the current design processes and assessment of performance of masonry structures. *Construct Build Mater*. 2013;41:990-1001.
3. Deb T, Yuen TY, Lee D, Halder R, You YC. Bi-directional collapse fragility assessment by dfem of unreinforced masonry buildings with openings and different confinement configurations. *Earthquake Eng Struct Dyn*. 2021;50(15):4097-4120.
4. Giambanco G, La Malfa Ribolla E, Spada A. Meshless meso-modeling of masonry in the computational homogenization framework. *Meccanica*. 2018;53(7):1673-1697.
5. Kujawa M, Lubowiecka I, Szymczak C. Finite element modelling of a historic church structure in the context of a masonry damage analysis. *Eng Fail Anal*. 2020;107:104233.
6. Lourenço PB. Computations on historic masonry structures. *Prog Struct Eng Mater*. 2002;4(3):301-319.
7. Macorini L, Izzuddin B. A non-linear interface element for 3d mesoscale analysis of brick-masonry structures. *Int J Numer Methods Eng*. 2011;85(12):1584-1608.
8. Malomo D, DeJong M. A macro-distinct element model (m-dem) for out-of-plane analysis of unreinforced masonry structures. *Eng Struct*. 2021;244:112754.
9. Spada A, Giambanco G, Rizzo P. Damage and plasticity at the interfaces in composite materials and structures. *Comput Methods Appl Mech Eng*. 2009;198(49–52):3884-3901.
10. Sutcliffe D, Yu H, Page A. Lower bound limit analysis of unreinforced masonry shear walls. *Comput Struct*. 2001;79(14):1295-1312.
11. Lourenço PJBB. *Computational Strategies for Masonry Structures*. Delft; 1997.
12. Andreotti G, Graziotti F, Magenes G. Detailed micro-modelling of the direct shear tests of brick masonry specimens: the role of dilatancy. *Eng Struct*. 2018;168:929-949.
13. Panto B, Silva L, Vasconcelos G, Lourenço PB. Macro-modelling approach for assessment of out-of-plane behavior of brick masonry infill walls. *Eng Struct*. 2019;181:529-549.
14. Ravichandran N, Losanno D, Parisi F. Comparative assessment of finite element macro-modelling approaches for seismic analysis of non-engineered masonry constructions. *Bull Earthq Eng*. 2021;19(13):5565-5607.
15. Lourenço PB, Rots JG. Multisurface interface model for analysis of masonry structures. *J Eng Mech*. 1997;123(7):660-668.
16. Abdulla KF, Cunningham LS, Gillie M. Simulating masonry wall behaviour using a simplified micro-model approach. *Eng Struct*. 2017;151:349-365.
17. Zeng B, Li Y, Noguez CC. Modeling and parameter importance investigation for simulating in-plane and out-of-plane behaviors of un-reinforced masonry walls. *Eng Struct*. 2021;248:113233.
18. Systemes D. Abaqus 6.14 Documentation–Theory Guide, Providence, RI; 2015.

19. Benzeggagh ML, Kenane M. Measurement of mixed-mode delamination fracture toughness of unidirectional glass/epoxy composites with mixed-mode bending apparatus. *Compos Sci Technol*. 1996;56(4):439-449.
20. Alfano G, Sacco E. Combining interface damage and friction in a cohesive-zone model. *Int J Numer Methods Eng*. 2006;68(5):542-582.
21. Andreotti G, Graziotti F, Magenes G. Expansion of mortar joints in direct shear tests of masonry samples: implications on shear strength and experimental characterization of dilatancy. *Mater Struct*. 2019;52(4):1-16.
22. Lotfi HR, Shing PB. Interface model applied to fracture of masonry structures. *J Struct Eng*. 1994;120(1):63-80.
23. Scimemi GF, Giambanco G, Spada A. The interphase model applied to the analysis of masonry structures. *Comput Methods Appl Mech Eng*. 2014;279:66-85.
24. Minga E, Macorini L, Izzuddin BA. A 3d mesoscale damage-plasticity approach for masonry structures under cyclic loading. *Meccanica*. 2018;53(7):1591-1611.
25. Xie Z, Sousamli M, Messali F, Rots J. A sub-stepping iterative constitutive model for cyclic cracking-crushing-shearing in masonry interface elements. *Comput Struct*. 2021;257:106654.
26. Chaimoon K, Attard MM. Modeling of unreinforced masonry walls under shear and compression. *Eng Struct*. 2007;29(9):2056-2068.
27. Citto C. *Two-Dimensional Interface Model Applied to Masonry Structures*. University of Colorado at Boulder; 2008.
28. Kumar N, Amirtham R, Pandey M. Plasticity based approach for failure modelling of unreinforced masonry. *Eng Struct*. 2014;80:40-52.
29. Kumar N, Barbato M. New constitutive model for interface elements in finite-element modeling of masonry. *J Eng Mech*. 2019;145(5):04019022.
30. Yuen TY, Deb T, Zhang H, Liu Y. A fracture energy based damage-plasticity interfacial constitutive law for discrete finite element modelling of masonry structures. *Comput Struct*. 2019;220:92-113.
31. Ortiz M, Popov EP. Accuracy and stability of integration algorithms for elastoplastic constitutive relations. *Int J Numer Methods Eng*. 1985;21(9):1561-1576.
32. Chaboche J, Cailletaud G. Integration methods for complex plastic constitutive equations. *Comput Methods Appl Mech Eng*. 1996;133(1–2):125-155.
33. Sloan SW, Abbo AJ, Sheng D. Refined explicit integration of elastoplastic models with automatic error control. *Eng Comput*. 2001;18:121-194.
34. Wilkins A, Spencer BW, Jain A, Gencturk B. A method for smoothing multiple yield functions. *Int J Numer Methods Eng*. 2020;121(3):434-449.
35. Nodargi NA, Bisegna P. State update algorithm for isotropic elastoplasticity by incremental energy minimization. *Int J Numer Meth Eng*. 2016;105:163-196. doi:10.1002/nme.4966
36. Nodargi NA, Bisegna P. A mixed finite element for the nonlinear analysis of in-plane loaded masonry walls. *Int J Numer Meth Eng*. 2019;120:1227-1248. doi:10.1002/nme.6179
37. Simo JC, Hughes TJ. *Computational Inelasticity*. Vol 7. Springer Science & Business Media; 2006.
38. Adhikary DP, Jayasundara CT, Podgorney RK, Wilkins AH. A robust return-map algorithm for general multisurface plasticity. *Int J Numer Methods Eng*. 2017;109(2):218-234.
39. Lee J, Bong HJ, Lee M-G. Return mapping with a line search method for integrating stress of the distortional hardening law with differential softening. *Comput Struct*. 2021;257:106652.
40. Pérez-Foguet A, Armero F. On the formulation of closest-point projection algorithms in elastoplasticity—part ii: globally convergent schemes. *Int J Numer Methods Eng*. 2002;53(2):331-374.
41. Abreu R, Mejia C, Roehl D. A comprehensive implicit substepping integration scheme for multisurface plasticity. *Int J Numer Methods Eng*. 2022;123(1):5-40.
42. Pech S, Lukacevic M, Füssl J. A robust multisurface return-mapping algorithm and its implementation in abaqus. *Finite Elem Anal Des*. 2021;190:103531.
43. Pérez-Foguet A, Rodríguez-Ferran A, Huerta A. Consistent tangent matrices for substepping schemes. *Comput Methods Appl Mech Eng*. 2001;190(35–36):4627-4647.
44. Sloan S. Substepping schemes for the numerical integration of elastoplastic stress–strain relations. *Int J Numer Methods Eng*. 1987;24(5):893-911.
45. Caballero A, Willam K, Carol I. Consistent tangent formulation for 3d interface modeling of cracking/fracture in quasi-brittle materials. *Comput Methods Appl Mech Eng*. 2008;197(33–40):2804-2822.
46. van der Pluijm R. Shear behaviour of bed joints. Proceedings of the 6th North American Masonry Conference; 1993:125-136; Technomic Publ. Co.
47. van der Pluijm R. Non-linear behaviour of masonry under tension. *Heron*. 1997;42:25-54.
48. Kaushik HB, Rai DC, Jain SK. Stress-strain characteristics of clay brick masonry under uniaxial compression. *J Mater Civil Eng*. 2007;19(9):728-739.
49. Grassl P, Rempling R. A damage-plasticity interface approach to the meso-scale modelling of concrete subjected to cyclic compressive loading. *Eng Fract Mech*. 2008;75(16):4804-4818.
50. Grassl P, Xenos D, Nyström U, Rempling R, Gylltoft K. Cdpm2: a damage-plasticity approach to modelling the failure of concrete. *Int J Solids Struct*. 2013;50(24):3805-3816.
51. Tao Y, Chen J-F. Concrete damage plasticity model for modeling frp-to-concrete bond behavior. *J Compos Constr*. 2015;19(1):04014026.
52. D'Altri AM, de Miranda S, Castellazzi G, Sarhosis V. A 3d detailed micro-model for the in-plane and out-of-plane numerical analysis of masonry panels. *Comput Struct*. 2018;206:18-30.

53. Sheikh AH, Bull PH, Kepler JA. Behaviour of multiple composite plates subjected to ballistic impact. *Compos Sci Technol*. 2009;69(6):704-710.
54. Chaimoon K. *Numerical Simulation of Fracture in Unreinforced Masonry*. UNSW; 2007.
55. Armero F, Pérez-Foguet A. On the formulation of closest-point projection algorithms in elastoplasticity—part i: the variational structure. *Int J Numer Methods Eng*. 2002;53(2):297-329.
56. Koiter WT. Stress-strain relations, uniqueness and variational theorems for elastic-plastic materials with a singular yield surface. *Q Appl Math*. 1953;11(3):350-354.
57. Crouch RS, Askes H, Li T. Analytical cpp in energy-mapped stress space: application to a modified drucker–prager yield surface. *Comput Methods Appl Mech Eng*. 2009;198(5–8):853-859.
58. Diana T. *Diana Finite Element Analysis user's Manual Release 9.4. 4*. Delft; 2012.
59. Atkinson R, Amadei B, Saeb S, Sture S. Response of masonry bed joints in direct shear. *J Struct Eng*. 1989;115(9):2276-2296.
60. Oliveira DV, Lourenço PB, Roca P. Cyclic behaviour of stone and brick masonry under uniaxial compressive loading. *Mater Struct*. 2006;39(2):247-257.
61. Vermeltfoort AT, Raijmakers T, Janssen H. Shear tests on masonry walls. Proceedings of the 6th North American Masonry Conference; 1993:183-1193; Technomic Publ. Co.
62. Ng CL. *Experimental and Theoretical Investigation of the Behaviour of Brickwork Cladding Panel Subjected to Lateral Loading*. University of Edinburgh; 1996.
63. Salmanpour AH, Mojsilović N, Schwartz J. Displacement capacity of contemporary unreinforced masonry walls: an experimental study. *Eng Struct*. 2015;89:1-16.
64. Messali F, Esposito R, Ravenshorst G, Rots J. Experimental investigation of the in-plane cyclic behaviour of calcium silicate brick masonry walls. *Bull Earthq Eng*. 2020;18(8):3963-3994.
65. Wilding BV, Dolatshahi KM, Beyer K. Shear-compression tests of URM walls: various setups and their influence on experimental results. *Eng Struct*. 2018;156:472-479.

SUPPORTING INFORMATION

Additional supporting information can be found online in the Supporting Information section at the end of this article.

How to cite this article: Nie Y, Sheikh A, Visintin P, Griffith M. A robust computational strategy for failure prediction of masonry structures using an improved multi-surface damage-plastic based interface model. *Int J Numer Methods Eng*. 2023;124(11):2498-2528. doi: 10.1002/nme.7218

APPENDIX A

THREE-DIMENSIONAL MODEL

Figure A1 displays the yield surfaces of the proposed model in 3D stress space.

$$\begin{Bmatrix}\sigma_n\\ \sigma_{s1}\\ \sigma_{s2}\end{Bmatrix}=\begin{bmatrix}1-D_n & 0 & 0\\ 0 & 1-D_s & 0\\ 0 & 0 & 1-D_s\end{bmatrix}\begin{Bmatrix}\sigma_n\\ \sigma_{s1}\\ \sigma_{s2}\end{Bmatrix}, \tag{A1}$$

$$\begin{Bmatrix}\sigma_n\\ \sigma_{s1}\\ \sigma_{s2}\end{Bmatrix}=\begin{bmatrix}K_n^0 & 0 & 0\\ 0 & K_s^0 & 0\\ 0 & 0 & K_s^0\end{bmatrix}\begin{Bmatrix}u_n\\ u_{s1}\\ u_{s2}\end{Bmatrix}, \tag{A2}$$

$$F_1=-\left(f_s-\overline{\sigma}_n\tan\phi\right)+\sqrt{\overline{\sigma}_{s1}^2+\overline{\sigma}_{s2}^2+\left(f_s-f_t\cdot\tan\phi\right)^2}, \tag{A3}$$

$$F_2=C_{nn}\overline{\sigma}_n^2+C_{ss}\left(\overline{\sigma}_{s1}^2+\overline{\sigma}_{s2}^2\right)+C_n\overline{\sigma}_n-f_c^2, \tag{A4}$$

$$Q_1=-\left(f_{sQ}-\overline{\sigma}_n\tan\phi_Q\right)+\sqrt{\overline{\sigma}_{s1}^2+\overline{\sigma}_{s2}^2+\left(f_{sQ}-f_t\cdot\tan\phi_Q\right)^2}, \tag{A5}$$

$$Q_2=F_2, \tag{A6}$$

$$dW_1^p = \begin{cases} \overline{\sigma}_n du_n^{p1} + \sqrt{\overline{\sigma}_{s1}^2 + \overline{\sigma}_{s2}^2}\sqrt{\left(du_{s1}^{p1}\right)^2 + \left(du_{s2}^{p1}\right)^2}, \sigma_n \geq 0, \\ \sqrt{\left(du_{s1}^{p1}\right)^2 + \left(du_{s2}^{p1}\right)^2}\left(\sqrt{\overline{\sigma}_{s1}^2 + \overline{\sigma}_{s2}^2} + \overline{\sigma}_n tan\phi\right), \sigma_n < 0, \end{cases} \tag{A7}$$

$$dW_2^p = \overline{\sigma}_n du_n^{p1} + \sqrt{\overline{\sigma}_{s1}^2 + \overline{\sigma}_{s2}^2}\sqrt{\left(du_{s1}^{p2}\right)^2 + \left(du_{s2}^{p2}\right)^2}. \tag{A8}$$

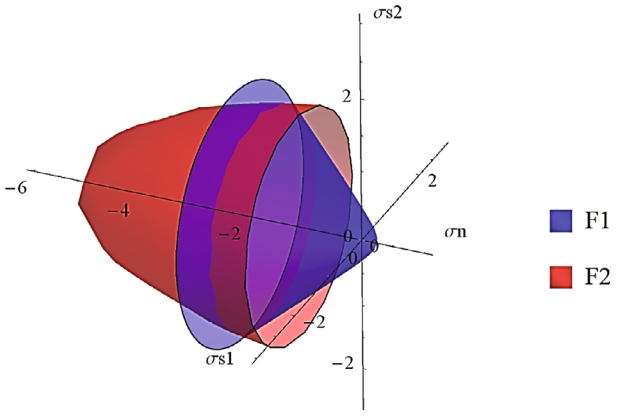

FIGURE A1 Yield surfaces of the proposed model in 3D stress space

APPENDIX B. NUMERICAL IMPLEMENTATION OF DAMAGE-PLASTIC MULTI-SURFACE MODEL

Algorithm B.1 Damage-Plasticity multi-surface model

1. Material properties and known variables

   $[K^0]$; $W_i^{p,t}$; $\{\sigma^t\}$;$\{du^{t+1}\}$;$[D^t]$ Compute: $tanf_Q(W_1^{p,t})$

2. Effective strength in time 't'

   $\{\bar{\sigma}^t\} = ([I] - [D^t])^{-1}\{\sigma^t\}$

3. Trial stress

   $\{^{trial}\,\bar{\sigma}^{t+1}\} = \{\bar{\sigma}^t\} + [K]\{du^{t+1}\}$

4. Determine trial yield surface set

   Compute: $f_{ch}{}^t = f_{ch}(W_2^{p,t})$; $\{F_{t+1}^{trial}\} = \begin{Bmatrix} F_1(\{^{trial}\,\sigma^{t+1}\}, f_{t0}, f_{s0}) \\ F_2(\{^{trial}\,\sigma^{t+1}\}, f_{ch}{}^t) \end{Bmatrix}$;

   $\{\mathbb{J}_{act}^{trial}\} = \{i \in \{1,2\} \mid F_{i,t+1}^{trial} > 0\}$; $FAIL =$ **TRUE**

5. Elastic status

   IF ($\{\mathbb{J}_{act}^{trial}\} = \emptyset$) **THEN**

   $\{\bar{\sigma}^{t+1}\} = \{^{trial}\,\bar{\sigma}^{t+1}\}$; $W_i^{p,t+1} = W_i^{p,t}$; $d\lambda_i^{t+1} = 0$; $FAIL =$ **FALSE**; **GOTO** 8

   ENDIF

6. Plastic status. Initialize values for NR iteration

   $\{\sigma^{k=0}\} = \{^{trial}\,\bar{\sigma}^{t+1}\}$; $W_i^{p,k=0} = W_i^{p,t}$; $\{d\lambda^{k=0}\} = \{0\}$; $\{\mathbb{J}_{act}^{k=0}\} = \{\mathbb{J}_{act}^{trial}\}$

7. NR loop: **DO** k = 1, k_{max}

   Compute $f_{ch}{}^k$ and $\frac{\partial f_{ch}}{\partial W_2^p}$ at loop " k "; $\{F^k\} = \begin{Bmatrix} F_1(\{\sigma^k\}) \\ F_2(\{\sigma^k\}, f_{ch}{}^k) \end{Bmatrix}$; $\frac{\partial Q_i}{\partial\{\bar{\sigma}\}}$; $\{r^k\}$

   IF ($\|r^k\| <$ Tolerence) **THEN**

   $\{\bar{\sigma}^{t+1}\} = \{\bar{\sigma}^k\}$; $\{W^{p,t+1}\}$; $\{d\lambda^{t+1}\}$ incldues $\begin{cases} d\lambda_i{}^k, & i \in \{\mathbb{J}_{act}^k\} \\ 0, & i \notin \{\mathbb{J}_{act}^k\} \end{cases}$; $FAIL =$ **FALSE**; **GOTO** 8

   ENDIF

   Compute $\frac{\partial F_i}{\partial\{\bar{\sigma}\}}$; $\frac{\partial^2 Q_i}{\partial\{\bar{\sigma}\}^2}$; $\frac{\partial F_i}{\partial W_i^p}$; $\frac{\partial W_i^p}{\partial d\lambda_i}$; $\frac{\partial F_i}{\partial d\lambda_i}$; $[J^k]$; $\{\delta^k\}$; $\{d\lambda_i{}^{k+1}\}$

   IF ($\exists i \in \{1,2\}$ such that $d\lambda_i^{k+1} < 0$)

   Re-define active surface set as: $\{\mathbb{J}_{act}^{k+1}\} = \{i \in \{1,2\} \mid d\lambda_i^{k+1} > 0\}$

   KKT condition: $d\lambda_i^{k+1} = 0, i \notin \{\mathbb{J}_{act}^k\}$

   IF ($\{\mathbb{J}_{act}^{k+1}\} = \emptyset$) **THEN** $\{\mathbb{J}_{act}^{k+1}\} = \{\mathbb{J}_{act}^{trial}\}$

   CYCLE NR loop

   ENDIF

   Update: $\{\bar{\sigma}^{k+1}\} = \{\bar{\sigma}^k\} + \{\delta\bar{\sigma}^k\}$; $\{W^{p,k+1}\}$

   ENDDO NR loop

8. Check converge

   IF ($FAIL =$ **TRUE**) **THEN**

   $\{\sigma^{t+1}\} = \{\sigma^t\}$; $\{W^{p,t+1}\} = \{W^{p,t}\}$; $\{d\lambda^{t+1}\} = 0$

   Reduce the global time increment in Abaqus

   ELSE

   Update: $[D^{t+1}] = [D^t](\{W^{p,t+1}\})$; $\{\sigma^{t+1}\} = ([I] - [D^{t+1}])\{\bar{\sigma}^{t+1}\}$

   ENDIF

APPENDIX C. NUMERICAL IMPLEMENTATION OF ADAPTIVE SUB-STEPPING

The procedure of this adaptive sub-stepping can be implemented by Algorithm C1. In the step 3 of Algorithm C1, after determining the increment of relative displacement in sub-stepping scheme $\{du^m\}$, an elastoplastic procedure as shown in Algorithm C1 (steps 3–7) is activated.

Algorithm C.1 Adaptive sub-stepping scheme

1. Pre-defined: Δt_{min}; k_d; ζ
2. Initialization of sub-stepping
   $m = 1$; $t^{m=1} = 0$; $\Delta t^{m=1} = 1$; $\{\bar{\sigma}^{m=1}\} = \{\bar{\sigma}^t\}$; $W_i^{p,m} = W_i^{p,t}$;
3. Update sub-step time increment and trial stress
   $t^{m+1} = t^m + \Delta t^m$; $\{du^m\} = \Delta t^m \cdot \{du^{t+1}\}$

$\{\bar{\sigma}^m\}$; $W_i^{m,t}$; $\{du^m\}$	input →	NR iteration	output →	$\{\bar{\sigma}^{m+1}\}$; $W_i^{m+1,t}$; $FAIL$; k

IF ($FAIL$ == **TRUE**) **THEN**

$t_m = t_m - \Delta t_m$; $\Delta t_m = \zeta \cdot \Delta t_m$; **GOTO** 4

ELSE

$$\delta^m = \begin{cases} \sqrt{k_d}, & k = 0 \\ \max\left(\sqrt{\frac{k_d}{k}}, \zeta\right), & k \neq 0 \end{cases}; \quad \Delta t^{m+1} = \min\left(\delta^m \cdot \Delta t^m, 1 - t^m\right)$$

ENDIF

4. Check the stopping criteria

IF ($t^{m+1} = 1$) **THEN** " Converge "; $M = m$; $\{\bar{\sigma}^{t+1}\} = \{\bar{\sigma}^{m+1}\}$; $W_i^{p,t+1} = W_i^{p,m+1}$

IF ($\Delta t^{m+1} < \Delta t_{min}$.**AND.** $\delta^m < 1$) **THEN** " Diverge ";

RETRN the algorithm and reduce global level time increment

IF (FAIL == **FALSE**) **THEN** $m = m + 1$